

# Padé approximant approach for obtaining finite-temperature spectral functions of quantum impurity models using the numerical renormalization group technique

Žiga Osolin<sup>1</sup> and Rok Žitko<sup>1,2</sup>

<sup>1</sup>*Jožef Stefan Institute, Jamova 39, SI-1000 Ljubljana, Slovenia*

<sup>2</sup>*Faculty of Mathematics and Physics, University of Ljubljana, Jadranska 19, SI-1000 Ljubljana, Slovenia*

(Received 14 February 2013; published 28 June 2013)

We introduce an alternative approach for obtaining smooth finite-temperature spectral functions of quantum impurity models using the numerical renormalization group (NRG) technique. It is based on calculating first the Green's function on the imaginary-frequency axis, followed by an analytic continuation to the real-frequency axis using Padé approximants. The arbitrariness in choosing a suitable kernel in the conventional broadening approach is thereby removed and, furthermore, we find that the Padé method is able to resolve fine details in spectral functions with less artifacts on the scale of  $\omega \sim T$ . We discuss the convergence properties with respect to the NRG calculation parameters (discretization  $\Lambda$ ,  $z$ -averaging, truncation cutoff) and the number of Matsubara points taken into account in the analytic continuation. We test the technique on the single-impurity Anderson model and the Hubbard model (within the dynamical mean-field theory). For the Anderson impurity model, we discuss the shape of the Kondo resonance and its temperature dependence. For the Hubbard model, we discuss the inner structure of the Hubbard bands in metallic and insulating solutions at half-filling, as well as in the doped Mott insulator. Based on these test cases, we conclude that the Padé approximant approach provides improved results for spectral functions at low-frequency scales of  $\omega \lesssim T$  and that it is capable of resolving sharp spectral features also at high frequencies.

DOI: [10.1103/PhysRevB.87.245135](https://doi.org/10.1103/PhysRevB.87.245135)

PACS number(s): 71.27.+a, 75.20.Hr

## I. INTRODUCTION

A nonmagnetic host metal doped with magnetic impurities exhibits low-temperature anomalies in its thermodynamic and transport properties known as the Kondo effect.<sup>1-3</sup> The resistance of such materials has a minimum at finite temperature (the Kondo temperature,  $T_K$ ).<sup>1</sup> An unyielding mystery for a number of years, this “Kondo problem” of the resistance minimum was eventually theoretically explained by J. Kondo by showing that the perturbation theory in higher order applied to the  $s$ - $d$  exchange Hamiltonian includes logarithmically divergent terms.<sup>2</sup> The effective exchange interaction strength  $J$  is renormalized to larger values as the temperature is reduced: magnetic impurities are weakly interacting at high temperatures, but become strong electron scatterers on the scale of  $T_K$ .<sup>4-7</sup> The system behaves as a renormalized local Fermi liquid (FL) at low temperatures.<sup>8,9</sup> Accurate results for the temperature dependence of the anomalies in the thermodynamic properties were obtained by K. Wilson using a novel technique, the numerical renormalization group (NRG).<sup>10-14</sup> It consists in reducing the Hamiltonian for the pointlike impurity to its one-dimensional form, discretizing the continuum of conduction-band electrons in a logarithmic way around the Fermi level, rewriting the Hamiltonian in the form of a tight-binding chain with exponentially decreasing hopping matrix elements, and numerically diagonalizing the resulting Hamiltonian in an iterative way. The NRG results for the thermodynamics of the Kondo model were later confirmed by the Bethe ansatz approach, which provides an analytic solution to the problem.<sup>15-17</sup>

While thermodynamic properties are simple to compute using the NRG,<sup>10,12,18,19</sup> dynamical properties (spectral functions and various dynamical susceptibility functions) and transport properties (conductance, thermopower) require significantly

more effort.<sup>20-29</sup> There are two main difficulties. The first concerns the actual calculation of the raw spectral functions. A number of algorithmic improvements over the years have increased the reliability of the method,<sup>30-36</sup> also at finite temperatures.<sup>37</sup> Since the NRG calculations are performed for tight-binding chains of finite length, the raw spectral functions are represented as sets of weighted  $\delta$  peaks, and the second difficulty consists in obtaining a smooth continuous representation of the spectra. At zero temperature, one usually performs spectral broadening using a log-Gaussian kernel, which is well adapted to the logarithmic discretization grid.<sup>14</sup> With high-quality raw results and using the  $z$ -averaging trick, it is possible to obtain highly accurate final results with few overbroadening effects.<sup>36,38,39</sup> At finite temperatures, a simple log-Gaussian broadening kernel is not appropriate for  $\omega \lesssim T$  (in units of  $\hbar = k_B = 1$ ). Instead, on low-energy scales, one should switch to a Gaussian or Lorentzian kernel.<sup>40</sup> Even when smooth crossover functions are used to glue the broadening kernel for  $\omega \gtrsim T$  with that for  $\omega \lesssim T$ ,<sup>37</sup> the resulting spectral functions exhibit artifacts in the crossover frequency region that cannot be fully eliminated. It is thus desirable to devise new approaches for obtaining more accurate continuous representations of spectral functions.

Impurity problems have applications ranging from magnetically doped materials and heavy-fermion compounds,<sup>41,42</sup> electron transport in nanostructures (quantum dots,<sup>43-50</sup> carbon nanotubes,<sup>51</sup> molecules and single-atom transistors,<sup>52-55</sup> molecular magnets),<sup>56,57</sup> to spectra of single atoms probed using a scanning tunneling microscope (STM)<sup>58-60</sup> and dissipative two-state systems,<sup>61</sup> but their importance has also vastly increased in recent decades because they play a central role in the dynamical mean-field theory (DMFT) for strongly correlated electron materials.<sup>62-67</sup> In the DMFT, a lattice problem of correlated electrons (such as Hubbard model, periodical

Anderson model, or Kondo lattice model) is mapped onto an effective single-impurity problem subject to self-consistency conditions. The approach is based on the observation that in the limit of infinite dimensions or infinite lattice connectivity, the self-energy function  $\Sigma(\mathbf{k}, \omega)$  becomes purely local<sup>63</sup> and depends only on frequency  $\omega$ , not on momentum  $\mathbf{k}$ . In this limit the method is exact, but it is also a good approximation for three-dimensional and some two-dimensional systems where spatial correlations are less important. Many techniques have been used in the past to solve the effective impurity models, which is the most computationally demanding part of DMFT calculations. Presently, the most popular methods are exact diagonalization, quantum Monte Carlo, especially the continuous-time algorithm (CT-QMC),<sup>68–70</sup> and NRG. The QMC is a stochastic simulation that is numerically exact, but time consuming. The results for spectral functions are accumulated in bins defined on the Matsubara imaginary-frequency axis and to obtain the spectra on the real-frequency axis one has to perform an analytic continuation,<sup>71</sup> for instance using the maximum entropy method<sup>71</sup> or with Padé approximants.<sup>72,73</sup> This procedure is not without peril and high quality numerical results are required to obtain reliable spectra. The NRG, on the other hand, can provide the results directly on the real-frequency axis and is thus well adapted to study the very low temperature properties and various details in the spectra. At finite temperatures, the most vexing technical difficulty of the NRG is the broadening problem discussed previously. Since the DMFT consists of iteratively solving the effective impurity problem, the spectral function artifacts at  $\omega \sim T$  tend to amplify. This is particularly bothersome for calculations of transport properties<sup>74–76</sup> where the contribution to the integrals comes mostly from the frequency window  $\omega \in [-5T : 5T]$ . Another issue in the DMFT(NRG) approach is the calculation of the self-energy as the ratio of two Green's functions<sup>14,30</sup>

$$\Sigma_{\sigma}(z) = \frac{\langle\langle [d_{\sigma}, H_{\text{int}}]; d_{\sigma}^{\dagger} \rangle\rangle_z}{\langle\langle d_{\sigma}; d_{\sigma}^{\dagger} \rangle\rangle_z}, \quad (1)$$

where  $H_{\text{int}}$  is the interaction part of the Hamiltonian, while  $d_{\sigma}$  is the impurity-orbital annihilation operator. The main problem is that the causality requirement  $\text{Im}\Sigma(\omega + i\delta) < 0$  can be (slightly) violated at low temperatures around the Fermi level. Ironically, the difficulties occur at low temperatures and on low-frequency scale, i.e., in the regime which is commonly believed to be the strength of the NRG, while it performs rather better than expected on intermediate and high-temperature and frequency scales.

In this work, we explore an alternative approach to spectral function calculations at finite temperatures. We propose to calculate the Green's functions on the discrete set of the imaginary Matsubara frequencies and then (when necessary) compute the Green's function for real-frequency arguments by analytic continuation using the Padé approximants. Switching to the imaginary axis in the NRG may seem like a step in the wrong direction, but it is motivated by the following observations. (i) The NRG spectra are not affected by large stochastic errors like the Monte Carlo data. The fine details are therefore not lost and can be resolved by analytic continuation. (ii) One directly obtains both real and imaginary parts of the Green's function on the imaginary axis, thus

Kramers-Kronig transformations are no longer necessary. (iii) In the DMFT(NRG) loops, most steps of the calculation can be performed in the Matsubara space; an analytic continuation is only necessary to compute the hybridization function on the real axis, which is, however, immediately integrated over to obtain the discretization coefficients. (iv) There is less arbitrariness compared to the broadening approach.

The paper is structured as follows. In Sec. II, we describe the basic steps in the DMFT calculations, the NRG technique, and our implementation of the Padé approximation. In Sec. III, we test the method on single-impurity problems: we compute the temperature dependence of the spectral function of the resonant-level model and the single-impurity Anderson model, and compare various approaches. In Sec. IV, we extend this calculation with a self-consistency loop and study the Hubbard model at finite temperatures. We conclude by discussing the relative merits of the different techniques.

## II. METHOD

### A. Dynamical mean-field theory

The DMFT is based on the observation that in the limit of infinite dimensions  $\Sigma(\omega, \mathbf{k}) \rightarrow \Sigma(\omega)$ , which implies the possibility of exactly mapping the lattice problem onto a single impurity problem subject to self-consistency conditions.<sup>77–80</sup> Let us consider the Hubbard model<sup>81–83</sup>

$$H_{\text{Hubbard}} = \sum_{\mathbf{k}\sigma} (\epsilon_{\mathbf{k}} - \mu) c_{\mathbf{k}\sigma}^{\dagger} c_{\mathbf{k}\sigma} + U \sum_i n_{i\uparrow} n_{i\downarrow}, \quad (2)$$

describing a lattice of sites indexed by  $i$  which can be occupied by electrons with spin  $\sigma = \uparrow$  and  $\sigma = \downarrow$ . Here  $\epsilon_{\mathbf{k}}$  is the noninteracting band dispersion,  $\mu$  is the chemical potential, and  $U$  the Hubbard repulsion. Furthermore,  $c_{i\sigma} = 1/\sqrt{N} \sum_{\mathbf{k}} e^{i\mathbf{k}\cdot\mathbf{r}_i} c_{\mathbf{k}\sigma}$ , and  $n_{i\sigma} = c_{i\sigma}^{\dagger} c_{i\sigma}$  is the local occupancy.

In the DMFT, the information about the lattice structure is fully captured by the noninteracting density of states (DOS)

$$\rho_0(\epsilon) = \frac{1}{N} \sum_{\mathbf{k}} \delta(\epsilon - \epsilon_{\mathbf{k}}). \quad (3)$$

Using the Hilbert transform, one can compute the corresponding Green's function  $G_0(z)$  in the full complex plane:

$$G_0(z) = \int_{-\infty}^{\infty} \frac{\rho_0(\epsilon) d\epsilon}{z - \epsilon}. \quad (4)$$

For common lattices (such as Bethe, 2D, 3D, and infinite-dimensional cubic lattices, as well as for flat band), there exist analytic closed-form expressions for  $G_0(z)$ .

The Hubbard model maps onto the single-impurity Anderson model (SIAM):<sup>77–80,84–88</sup>

$$H_{\text{SIAM}} = \sum_{\mathbf{k}\sigma} (\epsilon_{\mathbf{k}} - \mu) f_{\mathbf{k}\sigma}^{\dagger} f_{\mathbf{k}\sigma} - \mu n + U n_{\uparrow} n_{\downarrow} + \sum_{\mathbf{k}\sigma} V_{\mathbf{k}} (f_{\mathbf{k}\sigma}^{\dagger} d_{\sigma} + \text{H.c.}), \quad (5)$$

where the operators  $f_{\mathbf{k}\sigma}$  annihilate an electron in the continuum bath and  $d_{\sigma}$  on the impurity site, while  $n = n_{\uparrow} + n_{\downarrow}$  with  $n_{\sigma} = d_{\sigma}^{\dagger} d_{\sigma}$ . The (complex) hybridization function  $\Delta$ ,

defined as

$$\Delta(z) = \sum_k \frac{|V_k|^2}{z - \epsilon_k}, \quad (6)$$

fully characterizes the coupling between the impurity and the continuum,<sup>89</sup> i.e., there can be different (but physically fully equivalent) descriptions in terms of the bath energies  $\epsilon_k$  and hopping constants  $V_k$ .

The quantity of main interest is the momentum-resolved Green's function

$$G_{\mathbf{k}\sigma}(z) = \langle\langle c_{\mathbf{k}\sigma}; c_{\mathbf{k}\sigma}^\dagger \rangle\rangle_z \quad (7)$$

and the corresponding spectral function

$$A_{\mathbf{k}\sigma}(\omega) = -\frac{1}{\pi} \text{Im} G_{\mathbf{k}\sigma}(\omega + i\delta). \quad (8)$$

They provide information about the electron dispersion in the presence of interactions and can be used to determine the thermodynamic and transport properties of the system within the linear response theory.<sup>74,75,90</sup> The output from the impurity solver is the local impurity self-energy  $\Sigma_\sigma(z)$ , which in the DMFT is taken to be equal to the lattice self-energy of the correlated electron problem, thus

$$G_{\mathbf{k}\sigma}(z) = \frac{1}{z + \mu - \epsilon_{\mathbf{k}} - \Sigma_\sigma(z)}. \quad (9)$$

The local ( $\mathbf{k}$ -averaged) lattice Green's function is then

$$\begin{aligned} G_{\text{loc},\sigma}(z) &= \frac{1}{N} \sum_{\mathbf{k}} \frac{1}{z + \mu - \epsilon_{\mathbf{k}} - \Sigma_\sigma(z)} \\ &= \int \frac{\rho_0(\epsilon) d\epsilon}{[z + \mu - \Sigma_\sigma(z)] - \epsilon} \\ &= G_0[z + \mu - \Sigma_\sigma(z)]. \end{aligned} \quad (10)$$

The DMFT self-consistency condition relates the local lattice Green's function and the hybridization function through

$$\Delta_\sigma(z) = z + \mu - [G_{\text{loc},\sigma}^{-1}(z) + \Sigma_\sigma(z)]. \quad (11)$$

The hybridization function is then used as the input to the impurity solver in the next step of the DMFT iteration. The calculation proceeds until two consecutive solutions for the local spectral function differ by no more than some chosen convergence criterium. The approach to self-consistency can be significantly accelerated using Broyden mixing, which can also be very efficiently used to control the chemical potential  $\mu$  in fixed occupancy calculations.<sup>91</sup>

## B. Numerical renormalization group

Wilson's NRG is a nonperturbative numerical renormalization group approach applied to quantum impurity problems.<sup>10</sup> The cornerstone of the method is the *logarithmic discretization* of the conduction band.<sup>10,32,36,92</sup> The infinite number of the continuum degrees of freedom is reduced to a finite number, making the numerical computation tractable. The discretization is chosen to be logarithmic because in the Kondo problem the excitations from each energy scale contribute equally to the renormalization of the effective exchange coupling.<sup>6</sup> The band is divided into slices of exponentially decreasing

width,

$$\begin{aligned} I_m^- &= [-\Lambda^{-m}, -\Lambda^{-(m+1)}]D, \\ I_m^+ &= [\Lambda^{-(m+1)}, \Lambda^{-m}]D, \end{aligned} \quad (12)$$

for holes and electrons, respectively, with  $m \geq 0$ . Here,  $D$  is the half-bandwidth, while  $\Lambda > 1$  is known as the *discretization parameter*. A complete set of wave functions is then constructed in each interval  $I_m^\pm$ , the first chosen so that it couples to the impurity, while other Fourier components are localized away from it; only the first wave function is retained, while all the others are dropped from consideration.<sup>10</sup> This approximation becomes exact in the  $\Lambda \rightarrow 1$  limit, but the accumulated experience with the method indicates that it is reliable even for very large  $\Lambda$  despite the seeming crudeness of the approximation.<sup>93</sup> The problem is then transformed to a tridiagonal basis using the Lanczos algorithm, the result being a tight-binding Hamiltonian, which is known as the *hopping Hamiltonian* or the *Wilson chain*. A number of improvements have been devised over the years. On one hand, it has been shown that it is advantageous to perform calculations for several interpenetrating discretization meshes and then average the results.<sup>23,32</sup> Such *z-averaging* (or *twist-averaging*) allows more accurate calculations at larger values of  $\Lambda$  since the discretization artifacts tend to largely cancel out for aptly chosen meshes. On the other hand, modified discretization schemes further reduce some systematic errors of the original Wilson's approach.<sup>32,36,92</sup> These improvements are crucial if the goal is to obtain accurate results.

The NRG calculations in this work have been performed with the "NRG Ljubljana" package,<sup>94</sup> which consists of two parts. The first is a MATHEMATICA program, which initializes the problem by performing the exact diagonalization of the initial Hamiltonian in a chosen symmetry-adapted basis, and by transforming the operators of interest to the eigenbasis. The calculations are performed using a computer algebra system, and the input to the program are expressions in the familiar second quantization notation.<sup>95</sup> All quantities are stored in the form of irreducible matrix elements, and the Wigner-Eckart theorem is used to take into account the symmetry properties. The second part of the package is the C++ code, which performs the iterative diagonalization. This consists of adding the Wilson chain sites one by one, each time constructing the Hamiltonian matrices in all invariant subspaces, diagonalizing them, and transforming all the necessary operator matrices. The full description at step  $N$  of the iteration corresponds to the effective behavior of the system on the temperature/energy scale  $\omega_N \sim \Lambda^{-N/2}$ . Since the Fock space grows exponentially along the chain, only a small part of the computed eigenstates are retained after each step. A convenient way to perform this truncation is to keep the states up to some suitable energy cutoff  $E_{\text{cutoff}}$  defined in terms of  $\omega_N$ . Alternatively, at most  $N_{\text{keep}}$  states are retained. The systematic error introduced by truncation is small due to the energy-scale separation property<sup>10,38</sup> of the quantum impurity models: the matrix elements between excitations of vastly different energy scales are very small. The dynamical quantities are computed using the spectral decomposition (Lehmann representation) for the eigenstates of the full Hamiltonian. The original approach was based on the observation by Sakai *et al.*<sup>22</sup> that as one proceeds

from one step to the next, the lowest few eigenstates split due to the interaction with the added shell states, while the intermediate lower levels do not show any essential change. The intermediate states thus form a good approximation of the eigenstates of the Hamiltonian in the infinite-chain limit. For problems where the high-energy spectral features depend on the low-energy behavior of the system, the spectral function has to be computed taking into account the reduced density matrix obtained from the density matrix of the low-energy fixed point.<sup>31,96–98</sup> It has been shown that a complete basis for the full Fock space of the problem can be defined by judiciously using the information from the discarded part of the NRG eigenstates.<sup>33,34</sup> This method does not suffer from overcounting of excitations and it fulfills the normalization sum rule.<sup>35</sup> At finite temperatures, this scheme can be improved by including the contributions to the density matrix from all NRG shells.<sup>37</sup> This full-density-matrix (FDM) approach is currently the most reliable method for computing the finite-temperature spectral functions using the NRG. In the DMFT applications, one is particularly interested in the self-energy  $\Sigma$ , which may be computed as the ratio<sup>30</sup>

$$\Sigma_\sigma(z) = \frac{F_\sigma(z)}{G_\sigma(z)}, \quad (13)$$

where

$$F_\sigma(z) = \langle\langle [d_\sigma, H_{\text{int}}]; d_\sigma^\dagger \rangle\rangle_z. \quad (14)$$

This is known as the self-energy trick (or  $\Sigma$  trick),<sup>30</sup> and it has recently also been implemented in QMC calculations.<sup>99</sup>

Since the hopping Hamiltonian is finite, the computed raw spectral functions are represented as a sum of  $\delta$  peaks:

$$A_{\text{NRG},\sigma}(\omega) = \sum_j w_{j,\sigma} \delta(\omega - \omega_{j,\sigma}). \quad (15)$$

Alternatively, one may use fine-grained binning of these delta peaks into very narrow intervals on a logarithmic grid (for instance 1000 bins per frequency decade). To obtain a meaningful continuous function, these peaks need to be broadened. The original approach to obtaining a smooth curve was by Gaussian broadening followed by separate spline interpolation of the results in odd and even steps, and averaging of the two curves.<sup>22</sup> A better approach is broadening by the log-Gaussian distribution function:<sup>40</sup> each data point (delta peak at  $\omega_j$ ) is smoothed into

$$F(\omega, \omega_j) = \frac{e^{-b^2/4\theta(\omega\omega_j)}}{b\sqrt{\pi}} \exp\left(-\frac{\ln^2|\omega/\omega_j|}{b^2}\right), \quad (16)$$

i.e., a Gaussian function on the logarithmic scale, where  $b$  is the *broadening parameter*, chosen depending on the value of the discretization parameter  $\Lambda$  and the number of interleaved discretization meshes  $N_z$ . Peaks sharper than the width of the broadening kernel will appear broader than they truly are. Typically, the value of  $b$  is chosen to be 0.6 or less, but with large  $N_z$  and small  $\Lambda$  it can be much reduced, to the point of largely eliminating the NRG overbroadening problems (at the cost of much longer computation time).<sup>36,38</sup> At finite temperatures, the following broadening kernel has been proposed:<sup>37</sup>

$$K(\omega, \omega_j) = L(\omega, \omega_j)h(\omega_j) + G(\omega, \omega_j)[1 - h(\omega_j)], \quad (17)$$

where

$$\begin{aligned} L(\omega, \omega_j) &= \frac{\theta(\omega\omega_j)}{\sqrt{\pi}\alpha|\omega|} \exp\left[-\left(\frac{\ln|\omega/\omega_j|}{\alpha} - \gamma\right)^2\right], \\ G(\omega, \omega_j) &= \frac{1}{\sqrt{\pi}\omega_0} \exp\left[-\left(\frac{\omega - \omega_j}{\omega_0}\right)^2\right], \\ h(\omega_j) &= \begin{cases} 1, & |\omega_j| \geq \omega_0 \\ \exp\left[-\left(\frac{\ln|\omega_j/\omega_0|}{\alpha}\right)^2\right], & |\omega_j| < \omega_0 \end{cases}. \end{aligned} \quad (18)$$

Here  $\alpha$  is the broadening parameter for the log-Gaussian part, equivalent to  $b$  in the kernel in Eq. (16),  $\gamma = \alpha/4$ , while  $\omega_0$  is the cutoff where the log-Gaussian goes smoothly into the Gaussian part; typically,  $\omega_0$  is chosen to be of the order of the temperature  $T$ . This broadening approach leads to sizable artifacts on the scale of  $\omega_0$ . We find that in practice it is better to use a slightly modified kernel:

$$K(\omega, \omega_j) = L(\omega, \omega_j)h(\omega) + G(\omega, \omega_j)[1 - h(\omega)], \quad (19)$$

which differs only in the argument of the crossover function  $h$ . This breaks the normalization condition, but produces smoother spectra and the normalization is reestablished using the self-energy trick. This procedure still leads to a slight bump around  $\omega = \omega_0$ , which can be further smoothed out by averaging over several choices of  $\omega_0$ . The artifacts can, however, never be completely eliminated. In the following section, we therefore discuss an entirely different approach to obtaining a continuous spectral function at finite temperatures.

### C. Padé approximation

The Green's function  $G_\sigma(z)$  is related to its corresponding spectral function by

$$\text{Im}G_\sigma(\omega + i\delta) = -\pi A_\sigma(\omega) \quad (20)$$

and similarly for  $F_\sigma(z)$ . Instead of performing the broadening, the complex functions  $G_\sigma(z)$  and  $F_\sigma(z)$  (both analytic in the upper complex half-plane, cf. Titchmarsh's theorem) are evaluated at the Matsubara frequencies

$$i\omega_n = i(2n + 1)\pi T \quad (21)$$

via the Hilbert transform:

$$G_\sigma(i\omega_n) = \int_{-\infty}^{\infty} \frac{A_{\text{NRG},\sigma}(\omega)}{i\omega_n - \omega} d\omega, \quad (22)$$

and similarly for  $F_\sigma(i\omega_n)$ . Note that there is no need to perform the Kramer-Kronig transformation to calculate the real parts of  $G_\sigma(\omega)$  and  $F_\sigma(\omega)$ . Equation (22) is actually just a finite sum

$$G_\sigma(i\omega_n) = \sum_j \frac{w_{\sigma,j}}{i\omega_n - \omega_{\sigma,j}}. \quad (23)$$

If the  $z$  averaging is used, it is performed at this point:

$$G_\sigma(i\omega_n) = \frac{1}{N_z} \sum_{n=1}^{N_z} \sum_j \frac{w_{\sigma,j}^n}{i\omega_n - \omega_{\sigma,j}^n}. \quad (24)$$

The self-energy is calculated on the imaginary axis in the same way as on the real axis via Eq. (13), which holds in the whole upper complex half-plane. From the self-energy in the Matsubara frequencies  $\Sigma_\sigma(i\omega_n)$ , one calculates the local Green's function  $G_{\text{loc},\sigma}(i\omega_n)$  using Eq. (10). To complete the

DMFT loop, one needs to calculate the hybridization function on the real axis. We first calculate

$$\Delta_\sigma(i\omega_n) = i\omega_n + \mu - [G_{\text{loc},\sigma}^{-1}(i\omega_n) - \Sigma_\sigma(i\omega_n)]. \quad (25)$$

This function is analytic in the upper complex half-plane so we can perform an analytic continuation and evaluate  $\Delta$  just above the real axis to obtain the (real) hybridization function  $\Gamma_\sigma(\omega)$ :

$$\Gamma_\sigma(\omega) = -\text{Im}[\Delta_\sigma(\omega + i\delta)]. \quad (26)$$

An analytic continuation is also needed to determine the spectral function

$$A_\sigma(\omega) = -\frac{1}{\pi} \text{Im}[G_{\text{loc},\sigma}(\omega + i\delta)]. \quad (27)$$

The generalized mathematical problem of analytic continuation can be stated as follows: find an analytic function  $f(z)$  in the upper complex half-plane that coincides with calculated values on the discrete set of points

$$\{f(z_j) = f_j\}, \quad (28)$$

where  $(z_j, f_j)$  are the known point-value pairs of the function. The function  $f(z)$  must also obey the asymptotic behavior of the Green's function [or  $\Delta_\sigma(z)$ ], namely,

$$f(z) \sim \frac{1}{z}. \quad (29)$$

There exist two main numerical techniques for the analytic continuation: the maximum entropy method<sup>100,101</sup> (MEM) and Padé approximation.<sup>73</sup> MEM is essentially an improved fit to available data, taking into account known physical properties of the Green's/spectral function, such as sum rules, possible symmetries and higher moments of the distribution.<sup>100</sup> In this article, we focus on Padé approximation; the comparison of MEM and Padé in the context of NRG are yet to be explored.

The Padé approximation method is based on the assumption that  $f(z)$  is a rational function

$$f(z) = \frac{p_0 + p_1 z + \dots + p_{r-1} z^{r-1}}{q_0 + q_1 z + \dots + q_{r-1} z^{r-1} + z^r}, \quad (30)$$

where  $p_j$  and  $q_j$  are the unknown complex coefficients to be determined. We do not take any physical properties into account, thus the sum rules and symmetries can be violated. However, if the input points are accurate enough, we can expect possible violations to be small. Inserting the Padé approximant (30) into Eq. (28) for each point  $(z_j, f_j)$  generates a linear system of equations. Defining a vector of unknowns

$$\mathbf{x} = [p_0, p_1, \dots, p_{r-1}, q_0, q_1, \dots, q_{r-1}], \quad (31)$$

a right-hand-side vector

$$\mathbf{b} = [f_0 z_0^r, f_1 z_1^r, \dots, f_{2r-1} z_{2r-1}^r], \quad (32)$$

and a matrix

$$\mathbf{A} = \begin{pmatrix} 1 & z_0 & z_0^2 & \dots & z_0^{r-1} & -f_0 & -f_0 z_0 & \dots & -f_0 z_0^{r-1} \\ 1 & z_1 & z_1^2 & \dots & z_1^{r-1} & -f_1 & -f_1 z_1 & \dots & -f_1 z_1^{r-1} \\ \vdots & \vdots & \vdots & & \vdots & \vdots & \vdots & & \vdots \end{pmatrix}, \quad (33)$$

the solution for the coefficients is

$$\mathbf{x} = \mathbf{A}^{-1} \mathbf{b}. \quad (34)$$

We have assumed that the number of points  $(z_j, f_j)$  is  $2r$ . Alternatively, one can use recursive relations of the continued fractions representation of the Padé approximant to evaluate it at specific points.<sup>72</sup>

Fitting a rational function is a numerically ill-defined problem. Let us define  $\xi$  as the ratio between the biggest and the smallest element in the matrix  $\mathbf{A}$ . If  $z_j$  are the Matsubara frequencies, the ratio is approximately

$$\xi = [(4r + 1)\pi T]^{\pm r}, \quad (35)$$

where we take the minus sign in the power if the base is smaller than 1. In order to invert the matrix  $\mathbf{A}$ , the numeric precision of  $2 \log_2 \xi$  binary digits is needed,<sup>73</sup> i.e., much more than the standard 53-bit mantissa of 64-bit double-precision floating point numbers. For this reason, in our implementation of the Padé method, we use the GNU Multiple Precision Arithmetic Library (GMP) for arbitrary precision floating-point numerics. To solve the linear system of equations, we perform Gaussian elimination without pivoting. The process can be performed in  $O(r^3)$  multiplications. Each multiplication takes  $O(b \ln b)$  CPU cycles, where  $b$  is the number of mantissa bits in the floating point used (using fast Fourier transform multiplication).

When the coefficients of the Padé approximant are known to high precision, one can approximately calculate the value of the Green's function in any point of the upper complex half-plane using Horner's polynomial evaluation scheme. Most interesting is to use the values just above the real axis to compute the hybridization function  $\Gamma_\sigma(\omega)$  via Eq. (26) or the spectral function  $A_\sigma(\omega)$  via Eq. (27). The Padé approximant can be, however, also used for extrapolation when an insufficient number of Matsubara frequencies have been computed. It provides a good fit to tails even when the asymptotic behavior is not yet reached and simple asymptotic  $1/z$  fit on tails does not work.

In most calculations, we use  $N_m = 2r = 350$  Matsubara frequencies and internal matrix inversion precision of 1024 mantissa floating bits. In most cases, taking more points does not improve the solution; in fact, sometimes taking less points helps avoid some issues. The precision of input points plays a big role in how good the Padé approximant is, as already discussed in Ref. 73. We remark that one can also determine the coefficients of the rational function of order  $r$  using the data from more than  $N_m = 2r$  points by least-squares fitting.

### III. RESULTS FOR A SINGLE-IMPURITY PROBLEM: ANDERSON MODEL

We first consider a single impurity in a metal host described by the SIAM, now written as

$$H_{\text{SIAM}} = \sum_{k\sigma} \epsilon_k f_{k\sigma}^\dagger f_{k\sigma} + \epsilon n + U n_\uparrow n_\downarrow + \sum_{k\sigma} V_k (f_{k\sigma}^\dagger d_\sigma + \text{H.c.}), \quad (36)$$

where  $\epsilon$  is the impurity level, while the chemical potential is fixed to zero in this section,  $\mu = 0$ . The spectral function can

in general be expressed as

$$A(\omega) = -\frac{1}{\pi} \text{Im} \left( \frac{1}{\omega + i\delta - \epsilon - \Sigma(\omega) - \Delta(\omega)} \right). \quad (37)$$

When the continuum is modeled as a flat band, i.e., a band with a constant density of states  $\rho$  in the interval  $\omega \in [-D : D]$  which couples to the impurity with a constant hopping  $V_k \equiv V$  so that the hybridization strength

$$\Gamma = \pi \rho V^2 \quad (38)$$

is a constant, the complex hybridization function  $\Delta(z)$  is given as

$$\Delta(z) = -\frac{\Gamma}{\pi} \ln \left( \frac{z/D - 1}{z/D + 1} \right), \quad (39)$$

or, on the real-frequency axis for  $-D < \omega < D$ ,

$$\Delta(\omega + i\delta) = -\Gamma \left[ i + \frac{1}{\pi} \ln \left( \frac{1 - \omega/D}{1 + \omega/D} \right) \right]. \quad (40)$$

In the limit  $U = 0$ , the SIAM is equal to the noninteracting resonant-level model whose spectral function is given exactly by Eq. (37) with  $\Sigma(\omega) \equiv 0$ . For small  $\Gamma$ , the spectral function is well approximated by a Lorentzian

$$A(\omega) = \frac{\Gamma/\pi}{(\omega - \epsilon)^2 + \Gamma^2}. \quad (41)$$

For larger  $\Gamma$ , the hybridization self-energy effects become sizable, thus the curve shape deviates from a pure Lorentzian form, the peak is shifted to

$$\omega_0 = \epsilon - \frac{\Gamma}{\pi} \ln \left( \frac{1 - \omega_0/D}{1 + \omega_0/D} \right), \quad (42)$$

and, in addition, near the band edges  $\omega = \pm D$  the spectral function shows additional features: local minima at

$$\omega_{\min} = \pm D \sqrt{1 - \frac{2\Gamma}{\pi D}}, \quad (43)$$

and local maxima at  $\omega_{\max}$  given as the solutions of the equation

$$\pi(\omega_{\max} - \epsilon) + \Gamma \ln \left( \frac{1 - \omega_{\max}/D}{1 + \omega_{\max}/D} \right) = 0, \quad (44)$$

located near the band edges. For  $\epsilon = 0$  and moderately large  $\Gamma$ , they are approximately equal to

$$\omega_{\max} = \pm \left[ 1 - \exp \left( -\frac{\pi D}{\Gamma} \right) \right], \quad (45)$$

i.e., the maxima are located exponentially close to the band edges. Beyond  $\omega_{\max}$ , the spectral function goes to zero at  $\omega = \pm D$  in a continuous way, but with a diverging slope. Similar behavior is expected in all models where the imaginary part of the hybridization function drops to zero discontinuously, so that its real part (Hilbert transform) has a logarithmic singularity. This is the case, for example, for a 2D cubic lattice DOS with

$$\Delta(z) = \frac{2\Gamma D}{\pi^2 z} K(D^2/z^2), \quad (46)$$

where  $K$  is the elliptic function. The weight of the band-edge features is exponentially small for small  $\Gamma$ , but may be appreciable for moderate  $\Gamma$  of the order of the bandwidth, or if

the main spectral peak is close to the band edge (for instance, a few times  $\Gamma$ ). Such features typically are not visible in the NRG results because of the overbroadening effects, although in a careful calculation with small broadening width and for many values of the twist parameter  $z$ , they may be observed.<sup>36</sup> In the other case, when  $\text{Im}\Delta$  goes to zero continuously, the spectral function decreases monotonously near the band edges. We note that in noninteracting models, the spectral function does not depend on the temperature.

Unless otherwise noted, the NRG calculations in this section are performed with the discretization parameter  $\Lambda = 2$ , with the  $z$  averaging over  $N_z = 16$  values of the twist parameter using a modified discretization scheme which eliminates the band-edge artifacts of the conventional approach (nonadaptive type).<sup>36,92</sup> The high number of  $z$  values is important for the Padé approach and is further discussed in the following. Spectral functions are computed using the FDM NRG scheme and the  $\Sigma$  trick. The Wilson chain was sufficiently long so that the corresponding energy scale was smaller than any scale in the problem (including the temperature). The truncation cutoff is set at  $E_{\text{cutoff}} = 10\omega_N$ . Flat band with constant  $\Gamma$  is used in all cases.

### A. Noninteracting case, $U = 0$

Numerical calculation of a spectral function using the NRG is a nontrivial test of the method even in the absence of interactions. Clearly, the  $\Sigma$  trick would trivially produce the exact result. Nevertheless, there are other cases where the calculation of a spectral function cannot be improved by this trick (the  $T$ -matrix spectral function for the Kondo impurity model is a case in point), thus it is useful to perform a benchmark study of the directly computed (i.e., no  $\Sigma$  trick) spectral function for an exactly solvable noninteracting case. The conclusions about the broadening properties are relevant for a generic spectral function.

Even though the spectral function of a noninteracting problem does not depend on the temperature, numerical approaches generally have more or less severe difficulties reproducing this simple fact. In Fig. 1, we therefore first analyze the NRG results for the noninteracting resonant-level model obtained by the conventional broadening technique with a relatively small broadening parameter  $\alpha = 0.2$  and by the proposed Padé approximant method, and compare them with the exact result. We consider a peak centered at  $\omega = \epsilon = 0$ , i.e., at the Fermi level, where the NRG is said to have very good spectral resolution. In Fig. 1(a), we clearly observe the advantages of the Padé procedure at finite temperatures (here  $T = \Gamma$ ): the Padé approximant produces a spectral function which practically overlaps with the analytic formula, unlike the broadening procedure which produces a severely distorted spectral peak with missing spectral weight at low frequencies (the spectral peak tails are, however, well reproduced in both approaches; furthermore, we note that in the  $T \ll \Gamma$  limit, the broadening reproduces the exact results to a very good approximation on all frequency scales, thus the problems become manifest only at finite temperatures). In Fig. 1(b), we compare Padé approximant results obtained at different temperatures. The best agreement with the exact results is obtained for  $T \lesssim \Gamma$ , which is expected since for a temperature

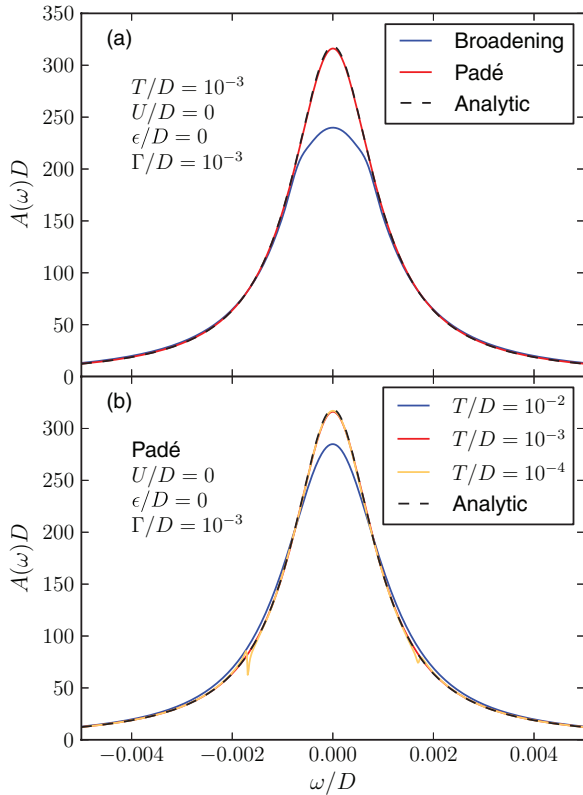


FIG. 1. (Color online) (a) Spectral function of the noninteracting resonant-level model obtained with broadening ( $\alpha = 0.2$ ) and with the Padé approximant. The Padé approximant overlaps nearly perfectly with the analytic result. (b) Spectral functions calculated at different temperatures  $T$  using the Padé approximant [i.e., using the sets of Matsubara points  $i\omega_n = i(2n + 1)\pi T$  with the raw results of NRG calculations performed at chosen temperatures  $T$ ]. The analytic result does not depend on the temperature. Deviations in the numerical results occur for  $T \gtrsim \Gamma$ .

scale comparable to the characteristic physical scales of the problem, the finite set of the Matsubara point provides a well matched sampling. For  $T \ll \Gamma$ , the agreement remains good but requires a sufficient number of the Matsubara points  $N_m$  (this issue is discussed in the following). Furthermore, for  $T = 10^{-4}$ , we observe some artifacts on the flanks of the curve (these are also discussed later on). For  $T \gg \Gamma$ , we find that the spectral height is underestimated also in the Padé approximant approach, but less severely than in the broadening scheme. This actually indicates a limitation of the NRG method itself, not of the Padé approximation scheme. Even at high  $T$  the Green's function at the corresponding Matsubara frequencies should contain the necessary information to reconstruct the Lorentzian peak, but the output from the NRG itself already has sizable systematic errors. We explore this question in more detail by plotting the raw Green's function on the Matsubara axis in panel (a) of Fig. 2 as well as the relative error in panel (b). The exact expression on the imaginary axis is (for  $\epsilon = 0$  and flat band)

$$G(iy) = -\frac{i}{y + \frac{\Gamma}{\pi} \arg\left(\frac{iy-D}{iy+D}\right)}. \quad (47)$$

We find that the systematic error of NRG is below 0.5%.

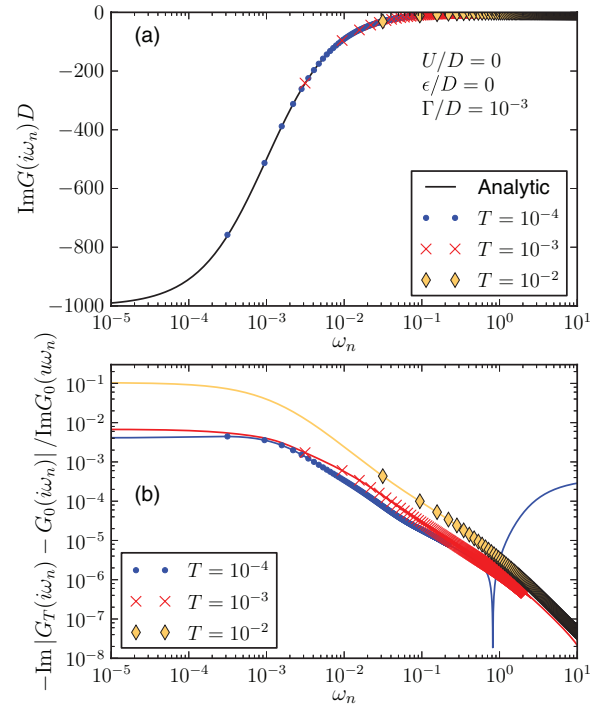


FIG. 2. (Color online) (a) Imaginary part of the Green's function for the noninteracting resonant-level model (same parameters as in Fig. 1) evaluated at the Matsubara frequencies for different temperatures. The analytic solution is shown with solid black line. (b) Relative errors of raw Matsubara spectral functions (dots) and the corresponding Padé approximants (solid lines). The dots quantify the intrinsic NRG errors, while the lines measure the full systematic error (intrinsic + analytic continuation errors).

We study the behavior near the band edges using the resonant-level model with a very large hybridization  $\Gamma/D = 0.3$ , see Fig. 3. The band-edge peaks are completely washed out in the broadening approach and the spectral function has long tails in the region where it should be equal to zero. The Padé approach resolves the band edges, although it is unable to correctly resolve the shape and the width of the near-band-edge resonances. Since the Padé approximant is a rational function,

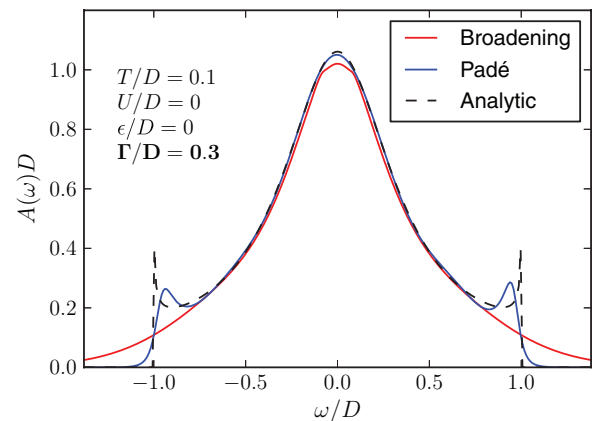


FIG. 3. (Color online) Spectral function of the noninteracting resonant-level model with large hybridization  $\Gamma/D = 0.3$ , where the behavior at the band edges  $\omega = -D$  and  $D$  may be compared.

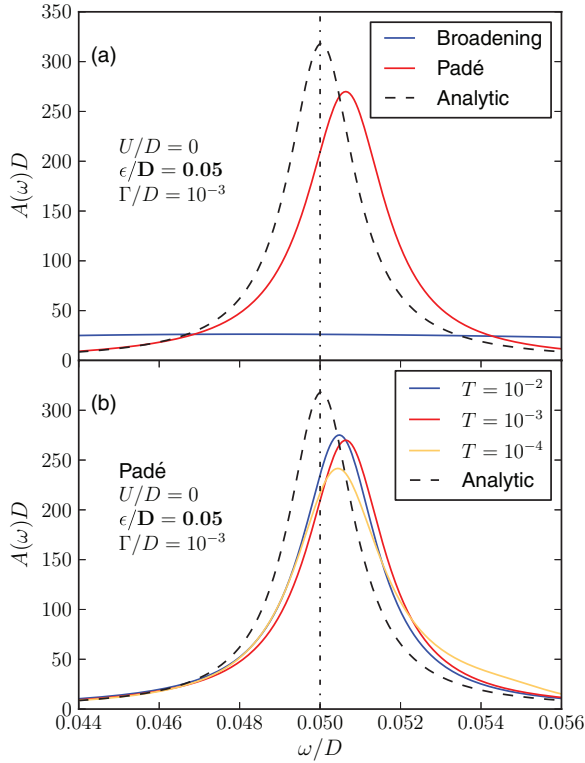


FIG. 4. (Color online) (a) Spectral function of the noninteracting resonant-level model with a peak centered far away from the Fermi level,  $\epsilon \gg \Gamma$ . Standard approach produces a severely overbroadened result since the kernel width for  $\alpha = 0.2$  is  $\Gamma_{\text{br}} \approx \alpha\epsilon = 10^{-2}$ . The Padé method is much more successful, although the peak is slightly shifted away from its correct position. (b) Comparison of the spectral functions computed with the Padé approximant for a range of temperatures. Similar degree of agreement is produced for all  $T$  considered.

it cannot describe a precipitous drop to zero at band edges. The Padé approach also better describes the behavior at the Fermi level, which is underestimated when broadening is used.

We now consider the asymmetric case where the spectral peak is located at  $\epsilon \neq 0$ , i.e., away from the Fermi level. This is the situation where the broadening procedure has notorious difficulties. The width of the log-Gaussian kernel is namely proportional to the frequency,

$$\Gamma_{\text{br}} \approx \alpha\omega \approx \alpha\epsilon, \quad (48)$$

where  $\alpha$  is the broadening parameter. If the intrinsic width of the spectral feature considered is much less than  $\Gamma_{\text{br}}$ , significant overbroadening will occur. In the example presented in Fig. 4, we take a rather extreme case of  $\Gamma/D = 10^{-3}$ , while  $\Gamma_{\text{br}}/D \approx 10^{-2}$  for  $\alpha = 0.2$  and  $\epsilon = 0.05$ . The plot in panel (a), indeed, shows that the broadening procedure produces a severely overbroadened peak, which is nearly a flat line on the scale of the figure. The Padé approximant, on the other hand, does not have difficulties reproducing narrow Lorentzian peaks, as expected. We find, however, that the peak is somewhat displaced from the correct position, and is slightly wider. In panel (b), we show that the spectral functions depend on the temperature in a nonsystematic way, although the result is acceptable for all temperatures considered. The deviations

from the exact results may again be related to the raw output from NRG, rather than to the Padé procedure.

The spectral function computed using Padé approximation is not guaranteed to fulfill the normalization sum rule. The Padé approach is a simple fitting procedure where the goal is to construct a rational function that exactly matches function values on a range of discrete (Matsubara) points, without any further constraints. There is no *a priori* reason for this function to be such that its integral on the real axis is normalized, since one is essentially performing an extrapolation. Nevertheless, we find that the results are rather satisfactory. For the peak centered at the Fermi level, the normalization deviates from 1 to at most a few per million. For a peak away from the Fermi level, the deviations can be sizable, up to several percent, especially for larger  $\Gamma$ . In principle, one could reformulate the Padé approximation as a least-squares-fitting procedure and implement the normalization sum rule (and perhaps additional higher-moment sum rules) as a constraint on the parameters. This is an idea worth pursuing. (If the self-energy trick is used, as for interacting models discussed in the following section, the normalization is recovered in the final result.)

## B. Interacting case, $U > 0$

We now turn to the interacting case with finite  $U$ . For  $U > \pi\Gamma$  and near half-filling, the system is in the Kondo regime.<sup>84,85,102</sup> As the temperature is reduced, on the temperature scale of  $U$ , the charge fluctuations on the impurity site freeze-out and the impurity may be described solely in terms of its spin degrees of freedom;<sup>7,12,103</sup> using the Schrieffer-Wolff transformation,<sup>103</sup> the model maps onto the Kondo impurity model

$$H_{\text{Kondo}} = \sum_{\mathbf{k}\sigma} \epsilon_{\mathbf{k}} f_{\mathbf{k}\sigma}^{\dagger} f_{\mathbf{k}\sigma} + J\mathbf{S} \cdot \mathbf{s}, \quad (49)$$

where the Kondo exchange coupling constant  $J$  is given by

$$\rho J = \frac{2\Gamma/\pi}{-\epsilon} + \frac{2\Gamma/\pi}{\epsilon + U}, \quad (50)$$

$\mathbf{S}$  is the impurity spin operator, while  $\mathbf{s}$  is the conduction-band spin density at the impurity position. At the Kondo temperature, given by<sup>12</sup>

$$T_K \sim U \exp\left(-\frac{1}{\rho J}\right), \quad (51)$$

the spin degree of freedom is screened by the conduction-band electrons (the Kondo effect). The two characteristic scales are also reflected in the spectral features: the charge fluctuations are associated with spectral peaks at  $\omega = \epsilon$  and  $\omega = \epsilon + U$  with half-width at half-maximum of  $2\Gamma$ , while the screening leads to a Kondo resonance<sup>104</sup> pinned to the Fermi level, with a spectral width of the order of the Kondo temperature. The zero-temperature spectral function at the Fermi level is determined by the Friedel sum rule<sup>105</sup>

$$A(0) = \frac{\sin^2 \delta_{\text{q.p.}}}{\pi\Gamma}, \quad (52)$$

where  $\delta_{\text{q.p.}}$  is the quasiparticle scattering phase shift in the local FL theory of the SIAM. If the system is particle-hole (p-h) symmetric, i.e., if  $\delta = \epsilon + U/2 = 0$ , then  $\delta_{\text{q.p.}} \equiv \pi/2$ , irrespective of the  $U/\Gamma$  ratio, thus there is a constraint

$\pi\Gamma A(0) = 1$ . In the deep Kondo regime,  $U/\pi\Gamma \gg 1$ , the phase shift is close to  $\pi/2$  even if the p-h symmetry is slightly broken. Unless  $\Gamma \ll D$ , we also expect some features near the band edges, just like in the noninteracting case, as discussed above. At finite temperatures, the Kondo resonance is washed out starting at  $T \sim T_K$ . In this work, we use the definition of  $T_K$  based on transport properties, i.e.,  $T_K$  is the temperature where the conductance through a nanodevice described by the SIAM is reduced to one-half the conductance quantum,  $G(T = T_K) = G_0/2$ . This definition was used by Hamann, Nagaoka, and Suhl; it is sometimes denoted as  $T_{K,H}$ . In addition, there is Wilson's thermodynamic definition  $\chi(T = T_{K,W})/(g\mu_B)^2 = 0.07$ , or the definition commonly used in the perturbation theory works, which is denoted as  $T_K^{(0)}$ . They are related through  $T_K^{(0)} = 0.4128T_{K,W}$  and  $T_{K,H} = 2.2T_{K,W}$ .

In Fig. 5, we plot the spectral functions in the p-h symmetric case for two different choices of  $U$  and  $\Gamma$ , but with the same  $\Gamma/U$  ratio. The curves obtained by broadening without the  $\Sigma$  trick are rather typical of standard NRG results: the Kondo resonance is well captured, but the Hubbard peaks are significantly over-broadened. For  $U/D = 1$ , the spectral density remains finite even far outside the conduction band due to the long tails of the broadening kernel. Furthermore, no features near the band edges are detected.

The curves obtained by the Padé approach are significantly improved even without the  $\Sigma$  trick. They show all the expected

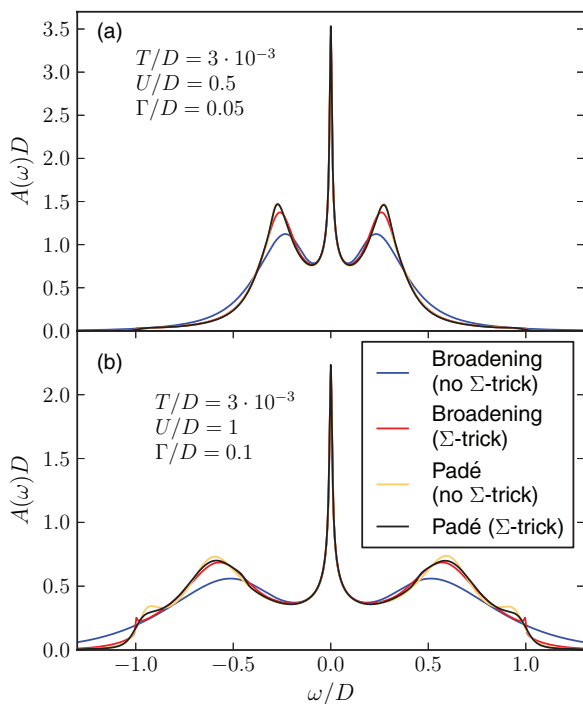


FIG. 5. (Color online) Spectral functions for the interacting single-impurity Anderson model (SIAM) obtained with broadening ( $\alpha = 0.2$ ) and by Padé approximation, with and without the  $\Sigma$  trick. Two sets of parameters with the same  $\Gamma/U$  ratio are used, thus the effective Kondo exchange coupling constant  $J$  is the same. For  $U/D = 1$ , the Hubbard peaks are located close to the band edges, and additional spectral features can be resolved at the edge. For  $U/D = 0.5$ , the Padé results with and without the  $\Sigma$ -trick overlap nearly perfectly, while for  $U/D = 1$  there are some small differences.

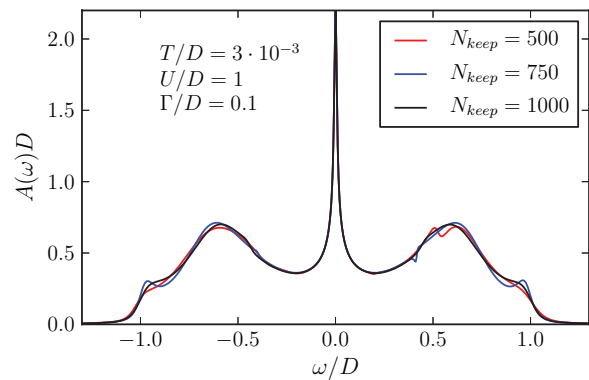


FIG. 6. (Color online) Spectral function of the single-impurity Anderson model for different numbers of kept states,  $N_{\text{keep}}$ , in the NRG procedure. The artifacts (for instance, the dip at  $\omega/D = 0.5$  for  $N_{\text{keep}} = 500$ ) are truncation-cutoff dependent, thus they stem from the raw NRG results.

features: the Kondo resonance, the Hubbard peaks, and (for  $U/D = 1$ ) the near-band-edge resonances, followed by a fast decay to zero outside the band.

When the  $\Sigma$  trick is used, the improvement is dramatic in the broadening approach, since the overbroadening is strongly reduced. For the  $U/D = 1$  case, the behavior near band edges is also improved. In the Padé approach, however, the use of the  $\Sigma$  trick has very little effect. We thus conclude that when the  $\Sigma$  trick is not used, the Padé approximant approach is better than broadening, and that the Padé approach reduces the need for using the self-energy trick. As discussed previously, the  $\Sigma$  trick is still very useful to restore the normalization of the spectral function to 1.

However, when using the Padé approximant we also observe some anomalies. Because they appear at different locations for different NRG truncation parameters, see Fig. 6, we argue that they are a direct manifestation of the systematic NRG errors that are reproduced too accurately by the Padé approximation. The standard broadening approach hides such anomalies, but they are, in fact, present in the spectra and may be revealed in “high-resolution” calculations with small broadening-kernel width. The Padé approximation, however, appears to overemphasize them. Improved results may be obtained by averaging over different truncation cutoffs.<sup>38</sup>

In the broadening approach, there is significant arbitrariness in the choice of the shape of the kernel, its width, and the approach to handle the  $\omega \lesssim T$  and  $\omega \gtrsim T$  parts in distinct ways. In the analytic continuation approach, there is, in principle, no arbitrariness, since the information about the Green's function on the set of Matsubara points fully and uniquely determines the Green's function in the whole complex half-plane, in particular on the real axis. The way the continuation is performed is, clearly, nonunique, but once the Padé approximation approach is chosen, the only adjustable parameter is the number of the Matsubara points taken into account in the fitting procedure. In QMC calculations, it is practice to use sufficiently many Matsubara frequencies to reach the asymptotic  $1/z$  behavior on the imaginary axis which corresponds to choosing  $\omega_{N_m} \gg U$ . (Note that the number of points is temperature dependent.) In NRG calculations, however, we observe that we can recover the tails using

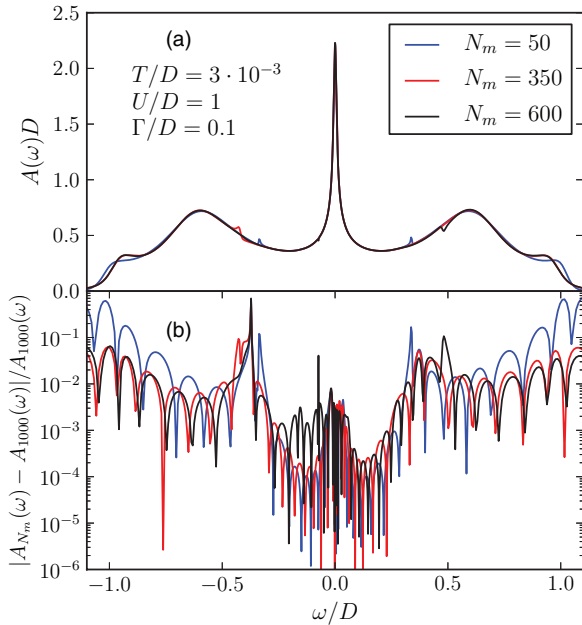


FIG. 7. (Color online) (a) Spectral functions of the single-impurity Anderson model obtained with Padé approximant using the first  $N_m$  Matsubara frequencies. (b) Relative difference between the spectral functions computed with  $N_m = 1000$  Matsubara frequencies compared to those for lower  $N_m$ .

less frequencies. The central peak is well reproduced using only  $N_m = 50$  frequencies and  $N_m = 350$  is enough to obtain essentially fully converged spectral function, as shown in Fig. 7(a). In Fig. 7(b), we plot the relative differences between the Padé approximants for different numbers of Matsubara points. In the Kondo peak region, the differences are below 0.01, thus the relative error contributed by the analytic continuation itself may be estimated to be well below one percent. From this, one may draw the conclusion that the main source of error at low frequencies in this approach is the systematic error of the NRG itself, not the analytic continuation procedure. At higher frequencies, the errors are slightly larger; in particular, at the artifacts discussed above the error may locally be up to 10%.

We find that the shift away from the real axis  $\delta$  in the expression for the spectral function  $A(\omega) = -(1/\pi)\text{Im}G(\omega + i\delta)$  does not play an important role, since typically there are no poles of the Padé rational function on the real axis (in which case it is, in fact, safe to put  $\delta = 0$ ). For large  $\delta$ , artificial broadening is introduced, see Fig. 8.

Of particular interest is the low-energy part of the spectral function, i.e., the Kondo resonance, because it is directly responsible for the conductance anomalies observed in magnetically doped metals and in semiconductor quantum dots. At nonzero temperatures, the shape of the resonance is difficult to reliably establish due to the broadening problems. Different version of the broadening procedure yield improved results in some cases, but worse in others. For example, an “optimized” scheme which produces less artifacts when there is a low-frequency spectral peak may lead to more pronounced artifacts in the case of a low-frequency spectral dip (and vice versa). There is thus no universal choice. The comparison in

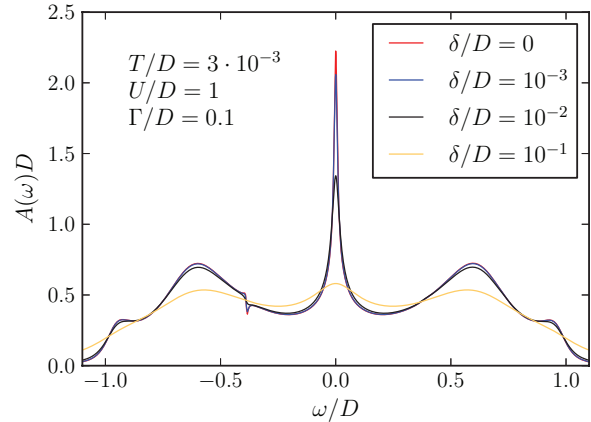


FIG. 8. (Color online) Spectral functions of the single-impurity Anderson model obtained with Padé approach using different shifts from the real axis.

Fig. 9, indicates that the Padé approximant approach does not create bumps near  $\omega = \pm T$ , unlike the broadening. In addition, it appears that broadening leads to a significant underestimation of the height of the spectral peak at its center. Using the  $\Sigma$  trick in the Padé approach fixes the normalization problem. Figure 9 illustrates one of the main results of this work: the Padé approximant approach allows to determine the finite-temperature spectral functions with *less artifacts* on the scale of  $\omega \sim T$ . The shape of the Kondo resonance is further discussed in Appendix A.

A function, analytic in the upper complex half-plane, is fully determined by its values on a countably infinite set of points. When fitting the Padé approximant, one commonly takes the values of the function at the Matsubara points  $i\omega_n$  for a finite number  $N_m$  of consecutive values of the index  $n$ , i.e.,  $n = 1, 2, \dots, N_m$ . This is, however, not necessary, nor always optimal. In particular, when the temperature  $T$  is very low, the Matsubara points are very dense and the first  $N_m$  points do not necessarily contain enough information about the high frequency scales, thus it is not possible to reconstruct the full spectral function. In these circumstances, we find it convenient to increase the spacing to  $s$ , so that we use the

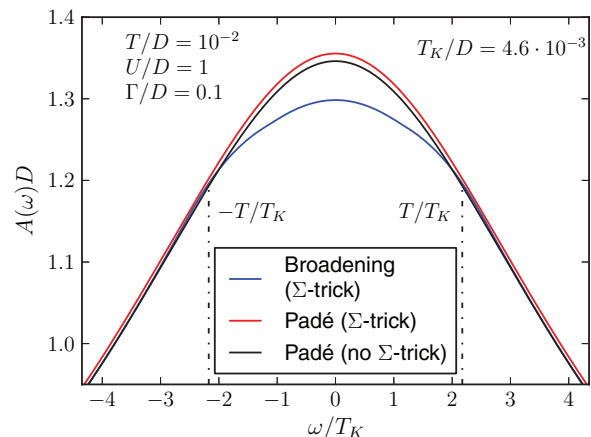


FIG. 9. (Color online) Close-up view of the top of the Kondo resonance at a temperature greater than  $T_K$ . Note the deviation of the peak shape from parabolic behavior when broadening is used.

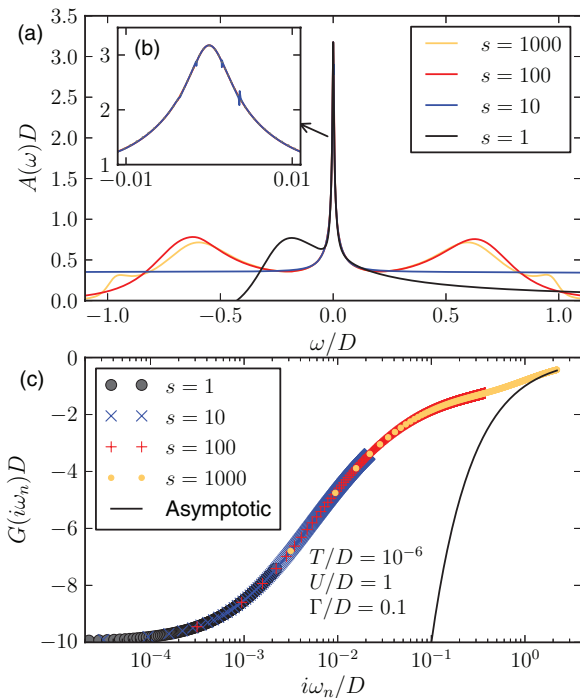


FIG. 10. (Color online) (a) Spectral functions of the SIAM at very low temperature obtained using Padé approximations, which use nonconsecutive Matsubara frequencies as input:  $i\omega_n = i(2n + 1)\pi sT$ . The parameter  $s$  quantifies the step length. The inset (b) shows a close-up on the Kondo resonance. (c) Green's function on the imaginary-frequency axis, indicating the Matsubara points taken into account in the Padé approximant construction. The black line is the asymptotic  $1/z$  form.

imaginary-frequency points

$$i\omega_n = i(2n + 1)s\pi T. \tag{53}$$

This corresponds to using the Matsubara points for a higher effective temperature  $sT$ , even though the raw spectral data were computed at the actual physical temperature  $T$ . The results of this procedure are illustrated in Fig. 10 for the case when the temperature is much below the lowest intrinsic temperature scale of the problem (here the Kondo temperature  $T_K = 4.6 \times 10^{-3}$ , thus  $T/T_K = 2 \times 10^{-4}$ ). For the standard choice of consecutive Matsubara points,  $s = 1$ , we find results that are clearly incorrect at high frequencies, even though the Kondo resonance appears to be well resolved. For  $s = 10$ , the Hubbard peaks are still not resolved, but for  $s = 100$ , they are well reproduced. Finally, for  $s = 1000$ , the spectral function is fully resolved, including the band-edge features. We note that for  $s = 1000$  the Matsubara points are chosen up to the asymptotic  $1/z$  tail of the Green's function, see Fig. 10(c). These results are very instructive, since they indicate that the information about the temperature is contained in the raw NRG results, not in the choice of the Matsubara frequencies. At low physical temperatures, it is thus perfectly safe to use high fictitious temperature in the Padé approximant calculation.

It is rather surprising that the Padé approximant produces smooth spectral functions with relatively little artifacts, given that the output from the NRG consists of a set of  $\delta$  peaks at excitations energies which tend to be clustered. We indeed

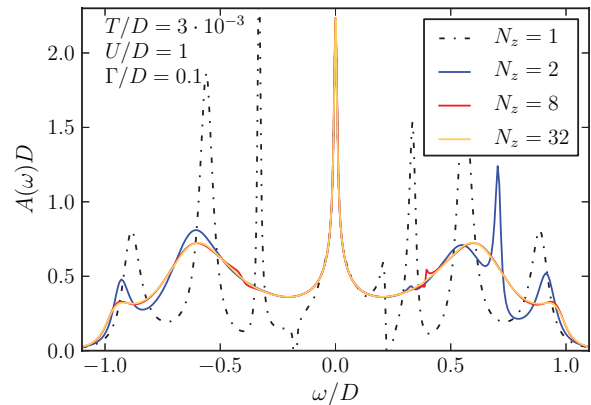


FIG. 11. (Color online) Spectral function of the SIAM for different number  $N_z$  of the  $z$ -averaging discretization meshes. For small  $N_z$ , the spectra exhibit a large number of spurious resonances, which are eliminated at larger  $N_z$ .

find that the Padé fitting applied to the results from a single NRG run with a specific discretization mesh (i.e.,  $N_z = 1$ ) produces meaningless results, see Fig. 11. However, already at  $N_z = 2$  the results are tremendously improved; the Kondo resonance, the Hubbard peaks, and the band-edge features are all resolved, located at the proper positions and with roughly correct spectral widths, although there are still sizable spurious spectral peaks. With finer  $z$  averaging, at  $N_z = 4$  and  $8$ , the results are almost converged with only some minor artifacts. At  $N_z = 32$  and beyond, we find no further improvement.

In Fig. 12, we study the convergence with respect to the NRG discretization parameter  $\Lambda$ . The continuum limit is restored for  $\Lambda \rightarrow 1$ , but practical calculations are only possible for  $\Lambda \gtrsim 1.5$ . We find that the artifacts are indeed reduced for smaller  $\Lambda$ , in particular, in the Hubbard peak region and near band edges. The form of the Kondo resonance is well described by all  $\Lambda$  in the range considered, but there appears to be a small yet systematic trend toward higher Kondo resonance height for smaller  $\Lambda$ . We have verified that the Kondo resonance is adequately described even for much higher  $\Lambda = 4$ , but the description of the Hubbard peaks becomes increasingly poor (results not shown).

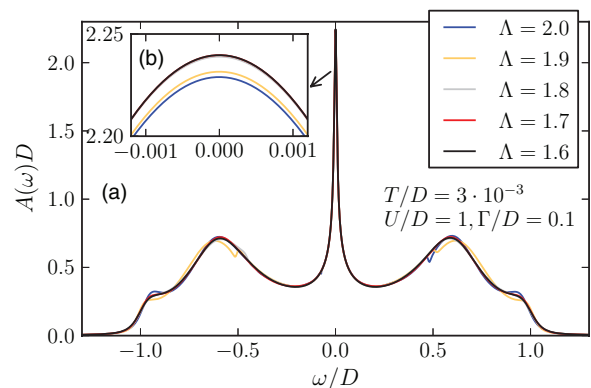


FIG. 12. (Color online) Spectral function of the SIAM for different values of the discretization parameters  $\Lambda$ .

### C. Dynamic susceptibilities

The spin and charge susceptibilities are defined as

$$\chi_s(z) = \langle\langle S_z; S_z \rangle\rangle_z, \quad \chi_c(z) = \frac{1}{4} \langle\langle n; n \rangle\rangle_z, \quad (54)$$

where  $S_z = (1/2)(n_\uparrow - n_\downarrow)$  and  $n = n_\uparrow + n_\downarrow$ ,  $n_\sigma$  being the impurity occupancy operators. We use units such that  $g\mu_B = 1$ , where  $g$  is the  $g$  ratio and  $\mu_B$  is the Bohr magneton, and we set the electron charge  $e = 1$ . The factor  $1/4$  in  $\chi_c$  is added for convenience to make the two susceptibilities equal in the noninteracting limit  $U = 0$  for the symmetric case.

For  $U = 0$ , the susceptibilities can be calculated exactly in terms of pair propagators

$$\begin{aligned} \Pi_{h\sigma'}^{p\sigma}(\omega) &= \frac{i}{2\pi} \int_{-\infty}^{\infty} G_\sigma(\omega + \omega') G_{\sigma'}(\omega') d\omega', \\ \Pi_{p\sigma'}^{p\sigma}(\omega) &= \frac{i}{2\pi} \int_{-\infty}^{\infty} G_\sigma(\omega - \omega') G_{\sigma'}(\omega') d\omega', \end{aligned} \quad (55)$$

as

$$\chi_s(\omega) = \frac{1}{2} \Pi_{h\downarrow}^{p\uparrow}(\omega), \quad \chi_c(\omega) = \frac{1}{2} \Pi_{p\downarrow}^{p\uparrow}(\omega). \quad (56)$$

The Green's functions here are time ordered, not retarded. The analytic expression in the wide-band limit are given in Ref. 106. For a finite flat band, they need to be computed numerically. Usually, we plot the imaginary parts denoted as  $\chi''(\omega) = \text{Im}[\chi(\omega)]$ , i.e., there is no  $-1/\pi$  factor as in the spectral function.

The Korringa-Shiba relation is a statement about the spin and charge dynamical susceptibilities in the low-frequency limit. It can be written as

$$\lim_{\omega \rightarrow 0} \frac{\text{Im}\chi(\omega)}{\omega} = p [\text{Re}\chi(0)]^2, \quad (57)$$

where  $p$  is a constant exactly equal to  $2\pi$  in the wide-band limit<sup>106,107</sup> ( $\Gamma, U \ll D$  in SIAM, or  $J \ll D$  in the Kondo model). For a band of finite width, the Korringa-Shiba relation takes a slightly different form.<sup>107</sup>

$$\lim_{\omega \rightarrow 0} \frac{\text{Im}\chi(\omega)}{\omega} = 2\pi [\text{Re}\langle\langle S_z; S_z + S_{\text{band}} \rangle\rangle_0]^2, \quad (58)$$

where  $S_{\text{band}}$  is the spin of the conduction-band electrons, thus the correlator on the right-hand side of Eq. (58) is the impurity magnetization induced by a small magnetic field applied to all electrons in the system.<sup>107</sup> (See Ref. 108 for a related discussion regarding the thermodynamic susceptibility and the Clogston-Anderson compensation theorem.) Alternatively, assuming proportionality between the magnetization in the impurity and in the band, one may work with Eq. (57) using an effective parameter  $p$ . For instance, for a noninteracting resonant-level model with  $\epsilon = 0$  and  $\Gamma/D = 10^{-1}$ , one finds  $p \approx 0.889 \times 2\pi$ , while for  $\Gamma/D = 10^{-2}$ ,  $p \approx 0.987 \times 2\pi$ . The correction to  $p/(2\pi)$  is thus approximately proportional to  $\Gamma/D$ .

We first test the calculation of susceptibilities on the  $U = 0$  model in the  $T \rightarrow 0$  limit, for a flat band with  $\Gamma/D = 10^{-2}$ . Spin and charge susceptibilities are the same in this case,  $\chi_s(\omega) = \chi_c(\omega)$ . In Fig. 13, we compare the NRG results for  $\chi''$  obtained with broadening and Padé, as well as the analytic results in the wide-band limit and for the actual flat band. We observe that the susceptibility function has a peak associated with the charge fluctuation scale of  $\Gamma$  and

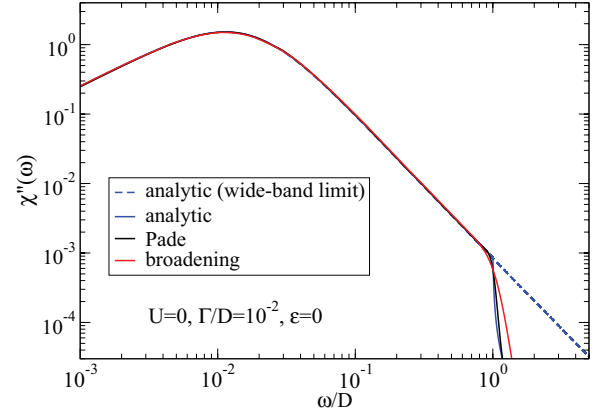


FIG. 13. (Color online) Dynamical charge susceptibility of the noninteracting resonant-level model computed with broadening and with the Padé continuation. We also compare analytic results for the wide-band limit ( $D \rightarrow \infty$ , dashed line) and finite flat band (full line),  $T/D = 10^{-4}$ .

a sharp drop at the band edge  $D$ . The analytic result obtained in the wide-band limit obviously does not account for the drop, which also explains the difference between the wide-band-limit coefficient  $2\pi$  and the effective coefficient  $p = 0.987 \times 2\pi$ . The two numerical results overlap to a high degree, except near the band edge where the Padé approximant better describes the sharp decrease. We find that the NRG result for the slope  $\text{Im}\chi(\omega)/\omega$  agrees within one per mil with the exact result, while  $\text{Re}\chi(0)$  obtained via the Kramers-Kronig transformation of  $\chi''$  has a one percent error. We thus obtain  $p = 0.967 \times 2\pi$ , which is two percent lower than the exact result. Of course,  $\text{Re}\chi(0)$  may be determined more accurately in NRG by other means.

In Fig. 14, we plot the dynamical spin and charge susceptibilities for the interacting SIAM in the Kondo regime for a range of temperatures. The charge susceptibility has a dominant peak on the scale of  $U$  (the maximum for  $T = 0$  is at  $\omega \approx 0.64U$ ), and a slight change of slope at the band edge  $\omega = D$ . The spin susceptibility has a dominant peak associated with spin fluctuations on the scale of  $T_K$ , a hint of a spectral feature at the frequency where the charge susceptibility has a maximum, and a drop at the band edge  $D$ . With increasing temperature (in the range  $T \sim T_K$ ), the charge susceptibility peak diminishes slightly, while the main peak in the spin susceptibility shifts to higher frequencies and decreases in magnitude.

For comparison, we also plot the spin susceptibility curves obtained using the broadening procedure in Fig. 15. The curves show artifacts at  $\omega \sim T$ , while Padé results feature a single well-defined peak, which is the expected result. Despite this improvement, we still observe some difficulties with the Padé approximant approach: it does not produce the expected slopes in the  $\omega \rightarrow 0$  limit [see, for example, the  $T/D = 3 \cdot 10^{-3}$  curve in Fig. 14(a)].

In order to determine the true origin of the problem, we study the raw binned data and plot the cumulant function

$$C(x) = \int_0^x \chi''_{\text{NRG}}(\omega) d\omega, \quad (59)$$

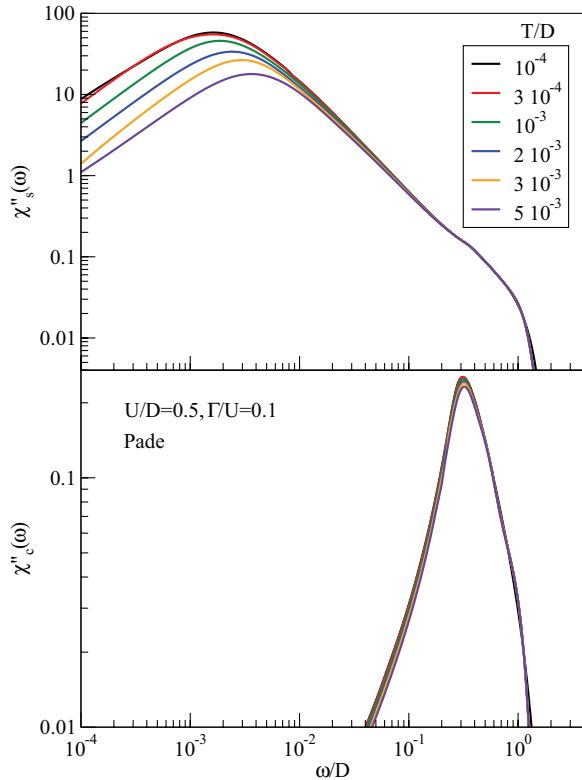


FIG. 14. (Color online) Dynamical spin (top) and charge (bottom) susceptibility of the single-impurity Anderson model obtained with Padé continuation for a range of temperatures. The Kondo temperature is  $T_K = 2.5 \cdot 10^{-3} D$ .

which is relatively smooth for large  $N_z$ . If  $\chi''(\omega)$  truly behaved linearly near  $\omega = 0$ , the cumulant should be quadratic for small  $x$ . We confirmed that this indeed holds to a good approximation for  $x$  somewhat lower than the lowest energy scale of the problem ( $\Gamma$  for the noninteracting case,  $T_K$  for the SIAM), see the  $T/D = 10^{-8}$  results in Fig. 16. However, for  $x$  much lower than the temperature  $T$ , the slope extraction becomes unreliable, see the  $T/D = 10^{-4}$  results. For small  $x$ , the cumulant is noisy and is not even positive in some intervals. This indicates that the Korringa-Shiba relation can only be

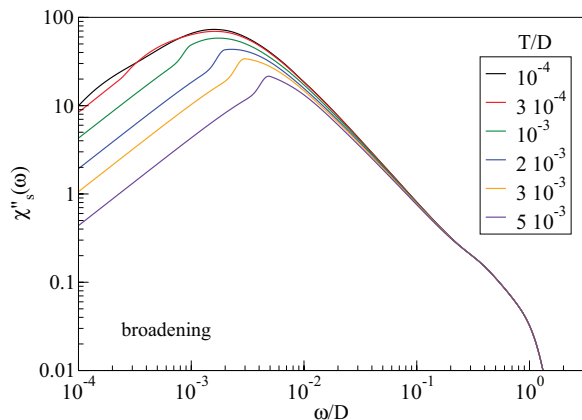


FIG. 15. (Color online) Dynamical spin susceptibility obtained using the broadening procedure (to be compared with the upper panel of Fig. 14).

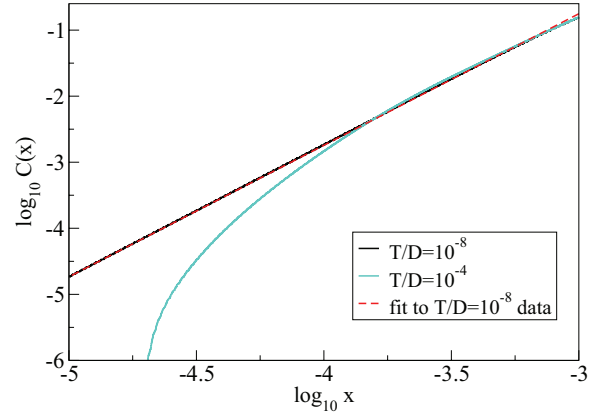


FIG. 16. (Color online) Cumulant function  $C(x)$  for the raw dynamical spin susceptibility spectral data. The slope of the fit function for  $T/D = 10^{-8}$  is 1.991.

tested in the  $T \ll \Gamma$  and  $T \ll T_K$  limits, respectively, but not for high temperatures where there is too much uncertainty. It also indicates that the raw dynamic information in the FDM NRG approach for  $\omega < T$  is not reliable. While this does not appear to be an issue for spectral functions, where the Padé approach produces what seems to be a reliable fit to the available raw data, this is not the case for dynamical susceptibilities where we observe incorrect slopes at low frequencies.

#### IV. RESULTS FOR A CORRELATED-ELECTRONS PROBLEM: HUBBARD MODEL WITHIN THE DMFT

We apply the Padé approximant approach to determine the spectral function of the Hubbard model in the paramagnetic phase within the DMFT. The questions of main interest are the following: (i) can we extend the upper limit of the temperature range where the DMFT(NRG) method can be safely applied towards  $T \sim D$  or even beyond? (ii) Can we obtain more detailed information about the internal structure of the Hubbard bands? (iii) Is the problem of causality violation at lower temperatures reduced?

We use the Bethe lattice with the noninteracting Green's function

$$G_0(z) = \frac{2}{D} \left[ \frac{z}{D} - i \operatorname{sgn}(\operatorname{Im}z) \sqrt{1 - \frac{z^2}{D^2}} \right]. \quad (60)$$

The DOS of the Bethe lattice shares some features with the 3D cubic lattice DOS. For instance, at the band edges it has square root singularities. The calculations are performed with  $N_z = 8$  and we take advantage of the Broyden mixing to improve the convergence.

We first discuss the half-filled system,  $\langle n \rangle = 1$ , which is particle-hole symmetric. The local spectral functions are shown in Fig. 17 for two different temperatures. For low and moderate interaction  $U$ , the behavior is qualitatively the same as in the non-self-consistent SIAM. The Kondo resonance at low frequencies is reinterpreted as the quasiparticle band and there are two Hubbard bands that now exhibit some internal structure, in particular, some enhancement at the inner band edges, which has also been resolved previously in the

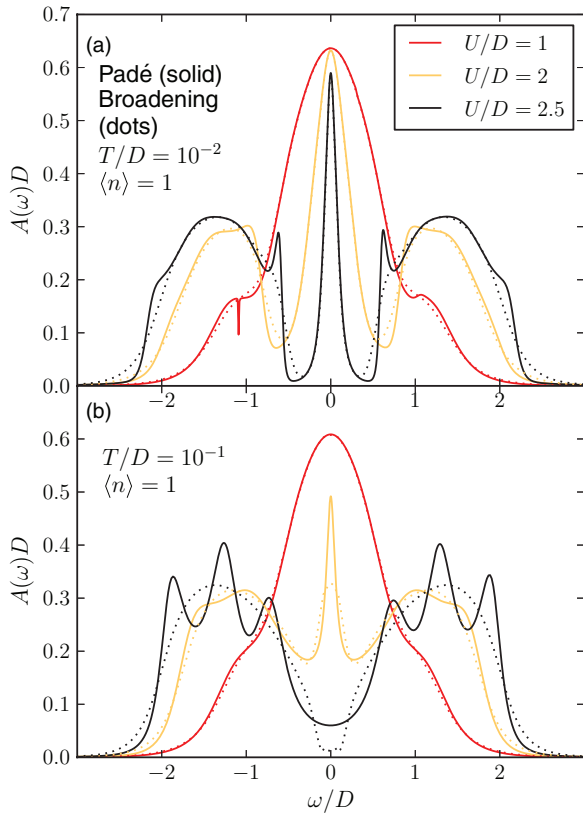


FIG. 17. (Color online) Spectral functions of the particle-hole symmetric Hubbard model at half-filling,  $\langle n \rangle = 1$ , at temperatures (a)  $T/D = 0.01$  and (b)  $T/D = 0.1$  for a range of repulsion strengths  $U/D$  computed using the dynamical mean-field theory (DMFT). We compare spectra computed using the Padé approach (solid lines) and with broadening (dots). (Padé continuation is used in all steps of the DMFT calculation, not just to obtain the final spectrum.)

broadening approach with very narrow kernels<sup>36</sup> and is known to be a real feature of the DOS;<sup>109,110</sup> see, for example, the  $U/D = 2.5$  curve at  $T/D = 10^{-2}$  in Fig. 17.

The spectra at higher temperature,  $T/D = 10^{-1}$ , are shown in the lower panel of Fig. 17. For values of  $U$  approaching the  $T = 0$  Mott metal-insulator transition, the quasiparticle peak is strongly suppressed and the spectral distribution inside the Hubbard bands is modified (see  $U/D = 2$  spectra). Broadening seems to underestimate the height of the quasiparticle peak in this regime. For larger  $U/D = 2.5$ , the quasiparticle peak is completely washed out and the Padé results suggest that the Hubbard bands develop a pronounced three peak structure. This is an artifact of the method and broadening results show no such structure.

In Fig. 18, we explore more carefully the reliability of the Padé approach in determining the internal structure of the Hubbard bands. In Fig. 18(a), we show a low-temperature result where the Padé approach at  $\Lambda = 2$  suggests, in addition to the well defined resonance at the inner band edge, also some feature at the outer Hubbard band edge. By reducing the discretization to  $\Lambda = 1.7$ , this feature is washed out, which indicates that it was an NRG artifact. This is a general recipe: real spectral features may be distinguished from artifacts by changing the NRG parameters (such as  $\Lambda$ , truncation

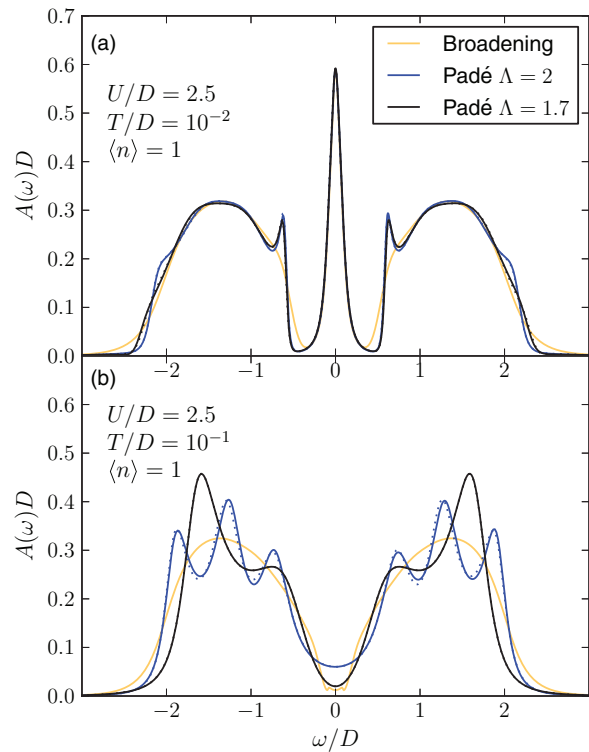


FIG. 18. (Color online) Spectral functions of the particle-hole symmetric Hubbard model at half-filling for  $U/D = 2.5$ : dependence on the NRG discretization parameter  $\Lambda$ . Dashed line show  $A(-\omega)D$ .

cutoffs, etc.), whereby real features should remain robust, while artifacts are very variable. This is well illustrated in Fig. 18(b), where the results confirm that the three-peak structure observed for  $U/D = 2.5$  at higher temperature is indeed an artifact.

We next consider a hole-doped Mott insulator with  $\langle n \rangle = 0.8$  at  $U/D = 4$ , see Fig. 19. This same parameter set has also been used in a recent study of the transport properties of this model, see Ref. 111. For low temperatures, we find very good agreement between broadening and Padé approaches for the low-frequency part of the spectra, while at high frequencies, the Padé approach reveals some internal structure of the upper Hubbard band, which can only be obtained in the broadening approach if the broadening parameter  $\alpha$  is much reduced. We note, however, that the integrated difference between two sequential Green's function in the DMFT loop does not go to zero in the Padé approach but rather oscillates around  $10^{-6}$ . This lack of true convergence can be shown to originate precisely in the inner structure of the upper Hubbard peak, which changes subtly from iteration to iteration. Such behavior is sometimes associated with physical instabilities of the system that are not allowed for in the DMFT ansatz, but may also here be an artifact. In any case, we believe that the upper Hubbard band does have internal structure and differs from simple noninteracting DOS.

We finally address the problems in the DMFT(NRG) at low temperatures, which manifest as the violation of the causality in the calculated self-energy functions, as discussed in the introduction. The self-energy has different asymptotic behavior than the hybridization function or the Green's

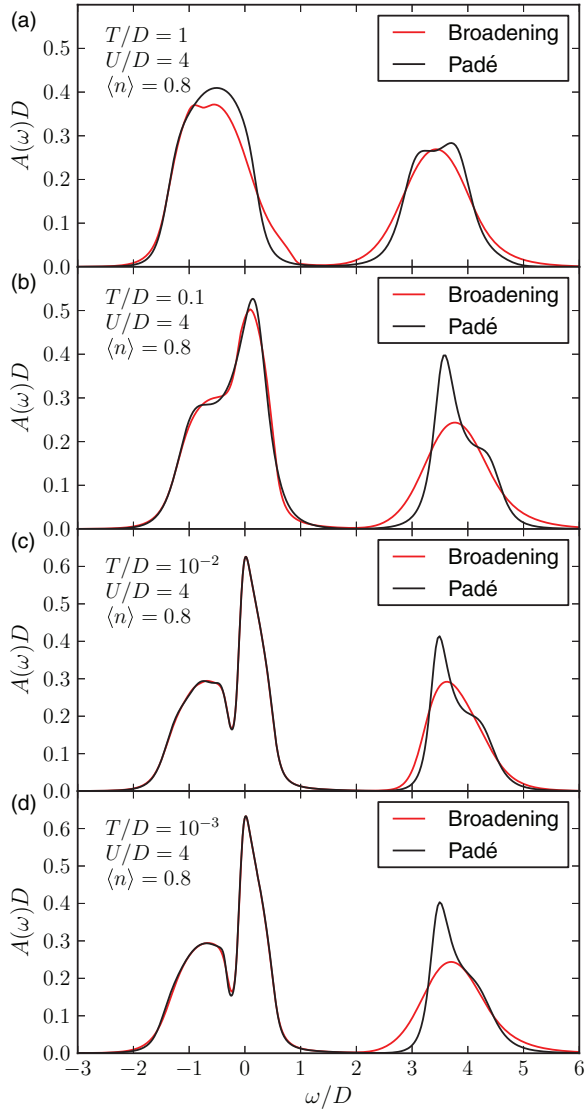


FIG. 19. (Color online) Spectral functions of the Hubbard model describing a doped Mott insulator for a range of temperatures. We show curves obtained by broadening ( $\alpha = 0.2$ ) and Padé approximation.

function, so special care must be taken when performing continuation with Padé. For large frequencies, it behaves as<sup>70</sup>

$$\Sigma(z) \sim U \langle n \rangle / 2 + O(1/z). \quad (61)$$

Because Padé requires  $O(1/z)$  asymptotic behavior, we first subtract  $U \langle n \rangle / 2$ , perform the continuation, and add the subtracted value back to the result. It was believed that since the self-energy is a ratio of two Green's function and the real parts need to be obtained by the Kramers-Kronig procedure, it was supposed that the (over)broadening of the spectral functions (imaginary parts) at high frequencies has an impact on all frequency scales in the real parts, thus spoiling the causality. This appears not to be the case, since in the Padé approximant approach the problems begin to show at the same temperature scale as with broadening. The causality violation thus appears to be intrinsic to the self-energy trick in NRG (i.e., is present already in the raw results). Interestingly, we did not observe

similar problems with the self-energy in calculations for the SIAM, but only in self-consistent DMFT calculations.

## V. CONCLUSION

We have analyzed a nonstandard approach for calculating finite-temperature spectral functions using the full-density-matrix numerical renormalization group (FDM NRG). It consists of evaluating the Green's function on the imaginary frequency axis, either at the Matsubara frequencies  $i\omega_n = i(2n+1)\pi T$  or at some other conveniently chosen set of points. To obtain the spectral function on the real frequency axis, an analytic continuation using the Padé approximant is performed. The technique works well in conjunction with sufficient  $z$  averaging, which partially removes the discretization artifacts of the NRG. Compared with the broadening approach, the technique does not have any arbitrariness in the choice of the broadening kernel and the only free parameter in most circumstances is the number of Matsubara points  $N_m$ ; the low-energy part of the spectral function converges quickly with increasing  $N_m$ . In addition, unlike with broadening, the spectral function does not have artifacts on the frequency scale of  $\omega \sim T$ . Some artifacts in spectral functions appear on high frequency scales and we have shown that their origin is in the raw NRG data, not in the analytic continuation procedure as such. A further advantage of the proposed technique is its capability to resolve narrow spectral features away from the Fermi level. We have also shown that the technique may be applied at relatively low temperatures by choosing instead of the Matsubara points a modified set of points on the imaginary axis, which provides a good sampling of the spectral information.

We have tested the method first on the single impurity Anderson model, where we have compared results of the new approach to the results obtained with broadening. We have also tested the approach on the Hubbard model within the DMFT. We find that the Padé approximant approach has some advantages over the broadening: (i) it has less spectral-function artifacts on the important scale of  $\omega \sim T$  and (ii) it can better resolve the inner structure of the Hubbard bands.

The main drawback of the Padé approximant method are the artifacts (e.g., complex spectra may give rise to additional spurious peaks) which, however, can be systematically eliminated by reducing  $\Lambda$  and increasing  $N_z$ . In addition, we find that while the Padé approach works well for spectral functions, it has more difficulties with reproducing correct slopes of dynamical susceptibilities at finite temperatures (which is an issue of NRG itself).

This work presents an alternative approach for obtaining smooth finite-temperature spectral functions for discrete data via Padé approximates, obviating the need to broaden discrete spectral functions. A possible improvement of our approach would be to build in as constraints additional information about the spectral function, such as the spectral moments, which are known with very high accuracy, and obtain the Padé approximant using an optimization procedure. One could also consider different fit functions. Work along these lines is in progress.

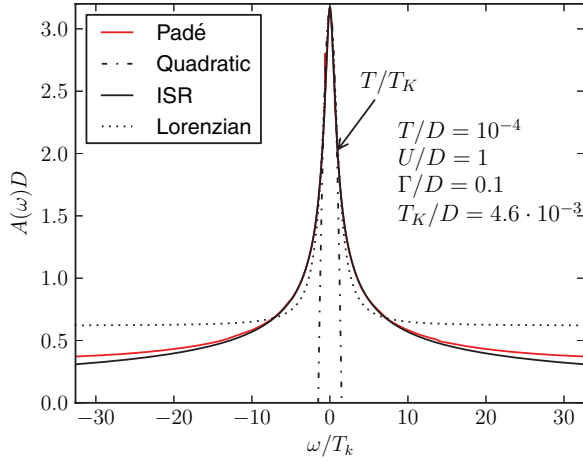


FIG. 20. (Color online) Shape of the Kondo resonance for  $T \ll T_K$ : close-up on the resonance peak and fits to various analytic expressions. ISR stands for the inverse-square-root (Frota) form.

### ACKNOWLEDGMENTS

We acknowledge discussions with Jernej Mravlje, Michele Fabrizio, and Thomas Pruschke and the support of the Slovenian Research Agency (ARRS) under Program P1-0044.

### APPENDIX A: KONDO RESONANCE

We now discuss the shape of the Kondo resonance, which is well known to deviate strongly from the Lorentzian form, see Fig. 20. The behavior near  $\omega = 0$  is parabolic, as expected for a regular FL system.<sup>1,8</sup> The quadratic fit, however, is only valid asymptotically for  $|\omega| \ll T_K$ . The fit to a Lorentzian function is valid in a somewhat wider energy interval, but it starts to deviate appreciably already at  $\omega \sim T_K$ . The long tails are better approximated by an inverse-square-root function (also known as the Doniach-Šunjić form),<sup>21,112,113</sup> as expected from the orthogonality-catastrophe physics for the scattering phase-shift  $\pi/2$ . The expression due to H. Frota is<sup>112</sup>

$$A(\omega) = \frac{1}{\pi\Gamma} \left[ \frac{1 + \sqrt{1 + (\omega/\Gamma_K)^2}}{2[1 + (\omega/\Gamma_K)^2]} \right]^{1/2}. \quad (\text{A1})$$

Using the local-moment approximation method, it has been shown that the tails are asymptotically logarithmic.<sup>114,115</sup>

At finite temperatures, the Kondo resonance can again be described by the Frota form using temperature-dependent parameters. We write

$$A(\omega, T) = \frac{h(T)}{\pi\Gamma} \left[ \frac{1 + \sqrt{1 + [\omega/\Gamma_K(T)]^2}}{2(1 + [\omega/\Gamma_K(T)]^2)} \right]^{1/2}. \quad (\text{A2})$$

For the temperature-dependent height, we find

$$h(T) = [1 + (2^{1/s} - 1)(rT/T_K)^p]^{-s}, \quad (\text{A3})$$

with  $s = 0.29$ ,  $p = 1.67$ , and  $r = 0.66$ , while for the width, we obtain

$$\Gamma_K(T) = cT_K [1 + a(T/T_K)^b], \quad (\text{A4})$$

with  $c = 0.60$ ,  $a = 1.97$ , and  $b = 1.33$ . This expression well describes the Kondo resonance in the parameter range

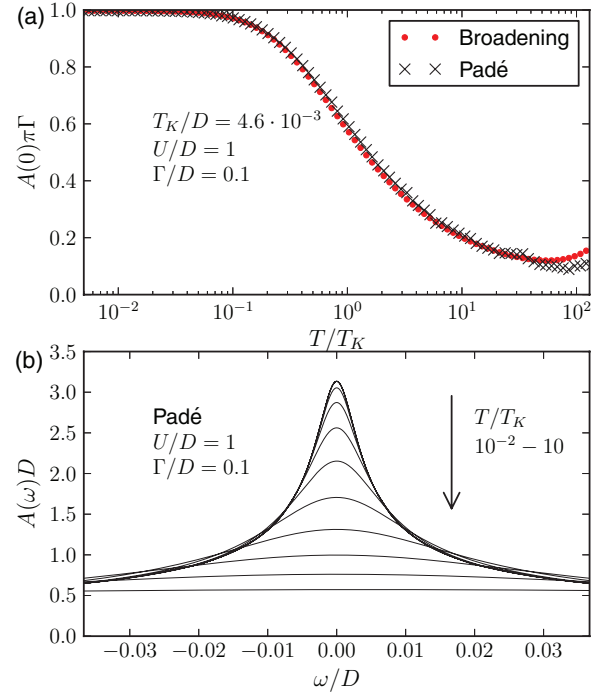


FIG. 21. (Color online) (a) Kondo resonance height as a function of temperature, calculated using broadening and Padé approximation. (b) Spectra for a range of temperatures from  $T/T_K = 10^{-2}$  to  $T/T_K = 10$  in 13 equally spaced temperatures in the logarithmic scale.

$|\omega| < 10T_K$  and  $T < 10T_K$ . Note that we do not fix  $p = 2$ , as required for a FL system. The  $T \rightarrow 0$  asymptotic behavior is thus incorrect. Our goal, however, is not the correct description of the asymptotic behavior (for which exact results are known anyway), but a better description on the crossover scale  $T \gtrsim T_K$ , which is more important for fitting experimental data.

We test how well the Friedel sum rule  $\pi\Gamma A(\omega = 0) = 1$  for the particle-hole symmetric case is fulfilled in the low-temperature limit. The results for  $\pi\Gamma A(\omega = 0, T)$  are shown in Fig. 21 on the logarithmic temperature scale. The sum rule at  $T \rightarrow 0$  is fulfilled within 0.0018 using the broadening approach, and within 0.0019 using the Padé approximant. The largest differences between the two approaches are in the

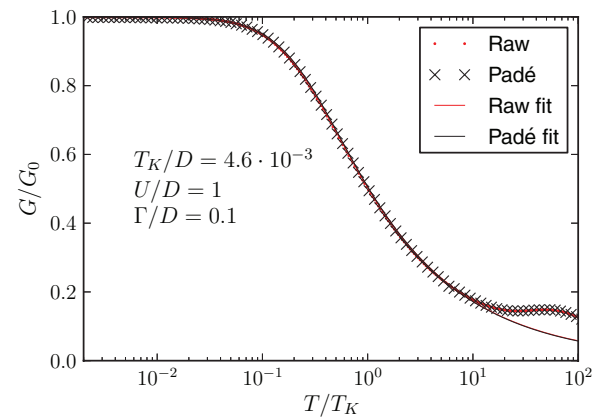


FIG. 22. (Color online) Conductance  $G(T)/G_0$  of a quantum dot described by the single-impurity Anderson model and a fit to the phenomenological Goldhaber-Gordon *et al.* formula.

intermediate temperature region where the height of the Kondo resonance is systematically underestimated by broadening.

### APPENDIX B: LINEAR CONDUCTANCE

We discuss an integrated spectral quantity, the conductance through a nanoscopic device (quantum dot) described by the SIAM, as given by the Meir-Wingreen formula:<sup>116</sup>

$$G(T) = G_0 \int_{-\infty}^{+\infty} d\omega \left( -\frac{\partial f}{\partial \omega} \right) \pi \Gamma A(\omega, T), \quad (\text{B1})$$

where  $G_0 = \frac{2e^2}{h}$  is the conductance quantum, and  $f$  is the Fermi-Dirac function. This quantity can be computed directly from raw spectral data, or using the continuous spectral function obtain either by broadening or by Padé method. We find that the results agree very well in all three cases, see Fig. 22. We fit them on the phenomenological function proposed by Goldhaber-Gordon *et al.*:<sup>44,54</sup>

$$G(T) = G_0 [1 + (2^{1/s} - 1)(T/T_K)^p]^{-s}. \quad (\text{B2})$$

Note that  $G(T_K) = G_0/2$ , in agreement with our definition of  $T_K$ . As discussed above, in a FL system, one may choose to fix  $p = 2$  in order to obtain the expected  $T \ll T_K$  asymptotics. For broadened spectra, we find

$$T_K = 4.4 \times 10^{-3}, \quad s = 0.229, \quad (\text{B3})$$

while for Padé spectra

$$T_K = 4.5 \times 10^{-3}, \quad s = 0.227. \quad (\text{B4})$$

The fitting was performed in the interval from  $T/T_K = 10^{-2}$  to 10. These values agree with the standard result  $s = 0.23$ .<sup>44</sup> Again, by relaxing the constraint  $p = 2$  a better fit is obtained in the intermediate temperature region where the crossover occurs. In this case, we find for broadened spectra,

$$T_K = 4.5 \times 10^{-3}, \quad s = 0.277, \quad p = 1.74, \quad (\text{B5})$$

while for Padé spectra,

$$T_K = 4.6 \times 10^{-3}, \quad s = 0.279, \quad p = 1.72. \quad (\text{B6})$$

Essentially, the same fit parameters are obtained if  $G(T)$  is computed directly by integrating the raw spectral data.

<sup>1</sup>A. C. Hewson, *The Kondo Problem to Heavy-Fermions* (Cambridge University Press, Cambridge, 1993).

<sup>2</sup>J. Kondo, *Prog. Theor. Phys.* **32**, 37 (1964).

<sup>3</sup>L. Kouwenhoven and L. Glazman, *Phys. World* **14**, 33 (2001).

<sup>4</sup>P. W. Anderson and G. Yuval, *Phys. Rev. Lett.* **23**, 89 (1969).

<sup>5</sup>P. W. Anderson, G. Yuval, and D. R. Hamann, *Phys. Rev. B* **1**, 4464 (1970).

<sup>6</sup>P. W. Anderson, *J. Phys. C: Solid St. Phys.* **3**, 2436 (1970).

<sup>7</sup>F. D. M. Haldane, *Phys. Rev. Lett.* **40**, 416 (1978).

<sup>8</sup>P. Nozières, *J. Low Temp. Phys.* **17**, 31 (1974).

<sup>9</sup>A. C. Hewson, *Phys. Rev. Lett.* **70**, 4007 (1993).

<sup>10</sup>K. G. Wilson, *Rev. Mod. Phys.* **47**, 773 (1975).

<sup>11</sup>H. R. Krishna-murthy, J. W. Wilkins, and K. G. Wilson, *Phys. Rev. Lett.* **35**, 1101 (1975).

<sup>12</sup>H. R. Krishna-murthy, J. W. Wilkins, and K. G. Wilson, *Phys. Rev. B* **21**, 1003 (1980).

<sup>13</sup>H. R. Krishna-murthy, J. W. Wilkins, and K. G. Wilson, *Phys. Rev. B* **21**, 1044 (1980).

<sup>14</sup>R. Bulla, T. Costi, and T. Pruschke, *Rev. Mod. Phys.* **80**, 395 (2008).

<sup>15</sup>N. Andrei, K. Furuya, and J. H. Lowenstein, *Rev. Mod. Phys.* **55**, 331 (1983).

<sup>16</sup>A. M. Tsvelick and P. B. Wiegmann, *Adv. Phys.* **32**, 453 (1983).

<sup>17</sup>A. M. Tsvelick and P. B. Wiegmann, *J. Phys. C: Solid State Phys.* **16**, 2321 (1983).

<sup>18</sup>L. N. Oliveira and J. W. Wilkins, *Phys. Rev. Lett.* **47**, 1553 (1981).

<sup>19</sup>W. C. Oliveira and L. N. Oliveira, *Phys. Rev. B* **49**, 11986 (1994).

<sup>20</sup>L. N. Oliveira and J. W. Wilkins, *Phys. Rev. B* **24**, 4863 (1981).

<sup>21</sup>H. O. Frota and L. N. Oliveira, *Phys. Rev. B* **33**, 7871 (1986).

<sup>22</sup>O. Sakai, Y. Shimizu, and T. Kasuya, *J. Phys. Soc. Jpn.* **58**, 3666 (1989).

<sup>23</sup>M. Yoshida, M. A. Whitaker, and L. N. Oliveira, *Phys. Rev. B* **41**, 9403 (1990).

<sup>24</sup>T. A. Costi and A. C. Hewson, *Phil. Mag. B* **65**, 1165 (1992).

<sup>25</sup>O. Sakai, Y. Shimizu, and T. Kasuya, *Prog. Theor. Phys.* **108**, 73 (1992).

<sup>26</sup>T. A. Costi and A. C. Hewson, *J. Phys.: Condens. Matter* **5**, L361 (1993).

<sup>27</sup>T. A. Costi, A. C. Hewson, and V. Zlatić, *J. Phys.: Condens. Matter* **6**, 2519 (1994).

<sup>28</sup>S. Andergassen, T. A. Costi, and V. Zlatić, *Phys. Rev. B* **84**, 241107 (2011).

<sup>29</sup>T. Rejec, R. Žitko, J. Mravlje, and A. Ramšak, *Phys. Rev. B* **85**, 085117 (2012).

<sup>30</sup>R. Bulla, A. C. Hewson, and T. Pruschke, *J. Phys.: Condens. Matter* **10**, 8365 (1998).

<sup>31</sup>W. Hofstetter, *Phys. Rev. Lett.* **85**, 1508 (2000).

<sup>32</sup>V. L. Campo and L. N. Oliveira, *Phys. Rev. B* **72**, 104432 (2005).

<sup>33</sup>F. B. Anders and A. Schiller, *Phys. Rev. Lett.* **95**, 196801 (2005).

<sup>34</sup>F. B. Anders and A. Schiller, *Phys. Rev. B* **74**, 245113 (2006).

<sup>35</sup>R. Peters, T. Pruschke, and F. B. Anders, *Phys. Rev. B* **74**, 245114 (2006).

<sup>36</sup>R. Žitko and T. Pruschke, *Phys. Rev. B* **79**, 085106 (2009).

<sup>37</sup>A. Weichselbaum and J. von Delft, *Phys. Rev. Lett.* **99**, 076402 (2007).

<sup>38</sup>R. Žitko, *Phys. Rev. B* **84**, 085142 (2011).

<sup>39</sup>A. Freyn and S. Florens, *Phys. Rev. B* **79**, 121102(R) (2009).

<sup>40</sup>R. Bulla, T. A. Costi, and D. Vollhardt, *Phys. Rev. B* **64**, 045103 (2001).

<sup>41</sup>P. Coleman, in *Lectures on the Physics of Highly Correlated Electron Systems VI*, edited by F. Mancini (American Institute of Physics, New York, 2002).

<sup>42</sup>J. W. Allen, *J. Phys. Soc. Jpn.* **74**, 34 (2005).

<sup>43</sup>L. I. Glazman and M. E. Raikh, *JETP Lett.* **47**, 452 (1988).

- <sup>44</sup>D. Goldhaber-Gordon, H. Shtrikman, D. Mahalu, D. Abusch-Magder, U. Meirav, and M. A. Kastner, *Nature (London)* **391**, 156 (1998).
- <sup>45</sup>D. Goldhaber-Gordon, J. Göres, M. A. Kastner, H. Shtrikman, D. Mahalu, and U. Meirav, *Phys. Rev. Lett.* **81**, 5225 (1998).
- <sup>46</sup>S. M. Cronenwett, T. H. Oosterkamp, and L. P. Kouwenhoven, *Science* **281**, 540 (1998).
- <sup>47</sup>W. G. van der Wiel, S. D. Franceschi, T. Fujisawa, J. M. Elzerman, S. Tarucha, and L. P. Kouwenhoven, *Science* **289**, 2105 (2000).
- <sup>48</sup>M. Pustilnik and L. Glazman, *J. Phys.: Condens. Matter* **16**, R513 (2004).
- <sup>49</sup>R. M. Potok, I. G. Rau, H. Shtrikman, Y. Oreg, and D. Goldhaber-Gordon, *Nature (London)* **446**, 167 (2007).
- <sup>50</sup>S. Andergassen, V. Meden, H. Schoeller, J. Splettstoesser, and M. R. Wegewijs, *Nanotechnology* **21**, 272001 (2010).
- <sup>51</sup>J. Nygard, D. H. Cobden, and P. E. Lindelof, *Nature (London)* **408**, 342 (2000).
- <sup>52</sup>J. Park, A. N. Pasupathy, J. I. Goldsmith, C. Chang, Y. Yaish, J. R. Petta, M. Rinkoski, J. P. Sethna, H. D. Abruna, P. L. McEuen *et al.*, *Nature (London)* **417**, 722 (2002).
- <sup>53</sup>W. Liang, M. P. Shores, M. Bockrath, J. R. Long, and K. Park, *Nature (London)* **417**, 725 (2002).
- <sup>54</sup>J. J. Parks, A. R. Champagne, T. A. Costi, W. W. Shum, A. N. Pasupathy, E. Neuscammen, S. Flores-Torres, P. S. Cornaglia, A. A. Aligia, C. A. Balseiro *et al.*, *Science* **328**, 1370 (2010).
- <sup>55</sup>G. D. Scott and D. Natelson, *ACS Nano* **4**, 3560 (2010).
- <sup>56</sup>C. Romeike, M. R. Wegewijs, W. Hofstetter, and H. Schoeller, *Phys. Rev. Lett.* **96**, 196601 (2006).
- <sup>57</sup>C. Romeike, M. R. Wegewijs, W. Hofstetter, and H. Schoeller, *Phys. Rev. Lett.* **97**, 206601 (2006).
- <sup>58</sup>V. Madhavan, W. Chen, T. Jamneala, M. Crommie, and N. S. Wingreen, *Science* **280**, 567 (1998).
- <sup>59</sup>N. Néel, J. Kröger, L. Limot, K. Palotas, W. A. Hofer, and R. Berndt, *Phys. Rev. Lett.* **98**, 016801 (2007).
- <sup>60</sup>H. Prüser, M. Wenderoth, P. E. Dargel, A. Weismann, R. Peters, T. Pruschke, and R. G. Ulbrich, *Nat. Phys.* **7**, 203 (2011).
- <sup>61</sup>A. J. Leggett, S. Chakravarty, A. T. Dorsey, M. P. A. Fisher, A. Garg, and W. Zwerger, *Rev. Mod. Phys.* **59**, 1 (1987).
- <sup>62</sup>W. Metzner and D. Vollhardt, *Phys. Rev. Lett.* **62**, 324 (1989).
- <sup>63</sup>E. Müller-Hartmann, *Z. Phys. B: Condens. Matter* **74**, 507 (1989).
- <sup>64</sup>G. Kotliar, *J. Phys. Soc. Japan* **74**, 147 (2005).
- <sup>65</sup>T. Maier, M. Jarrell, T. Pruschke, and M. H. Hettler, *Rev. Mod. Phys.* **77**, 1027 (2005).
- <sup>66</sup>G. Kotliar, S. Y. Savrasov, K. Haule, V. S. Oudovenko, O. Parcollet, and C. A. Marianetti, *Rev. Mod. Phys.* **78**, 865 (2006).
- <sup>67</sup>A. Georges, *Annalen der Physik* **523**, 672 (2011).
- <sup>68</sup>P. Werner, A. Comanac, L. de' Medici, M. Troyer, and A. J. Millis, *Phys. Rev. Lett.* **97**, 076405 (2006).
- <sup>69</sup>K. Haule, *Phys. Rev. B* **75**, 155113 (2007).
- <sup>70</sup>E. Gull, A. J. Millis, A. I. Lichtenstein, A. N. Rubtsov, M. Troyer, and P. Werner, *Rev. Mod. Phys.* **83**, 349 (2011).
- <sup>71</sup>M. Jarrell and J. E. Gubernatis, *Phys. Rep.* **269**, 133 (1996).
- <sup>72</sup>H. J. Vidberg and J. W. Serene, *J. Low Temp. Phys.* **29**, 179 (1977).
- <sup>73</sup>K. S. D. Beach, R. J. Gooding, and F. Marsiglio, *Phys. Rev. B* **61**, 5147 (2000).
- <sup>74</sup>M. Jarrell and T. Pruschke, *Phys. Rev. B* **49**, 1458 (1994).
- <sup>75</sup>M. Jarrell, J. K. Freericks, and T. Pruschke, *Phys. Rev. B* **51**, 11704 (1995).
- <sup>76</sup>C. Grenzbach, F. B. Anders, G. Czycholl, and T. Pruschke, *Phys. Rev. B* **74**, 195119 (2006).
- <sup>77</sup>A. Georges and G. Kotliar, *Phys. Rev. B* **45**, 6479 (1992).
- <sup>78</sup>A. Georges and W. Krauth, *Phys. Rev. Lett.* **69**, 1240 (1992).
- <sup>79</sup>M. J. Rozenberg, X. Y. Zhang, and G. Kotliar, *Phys. Rev. Lett.* **69**, 1236 (1992).
- <sup>80</sup>M. Jarrell, *Phys. Rev. Lett.* **69**, 168 (1992).
- <sup>81</sup>J. Hubbard, *Proc. R. Soc. London, Ser. A* **276**, 238 (1963).
- <sup>82</sup>J. Kanamori, *Prog. Theor. Phys.* **30**, 275 (1963).
- <sup>83</sup>M. C. Gutzwiller, *Phys. Rev. Lett.* **10**, 159 (1963).
- <sup>84</sup>P. W. Anderson, *Phys. Rev.* **124**, 41 (1961).
- <sup>85</sup>P. W. Anderson, *Phys. Rev.* **164**, 352 (1967).
- <sup>86</sup>P. W. Anderson, *Rev. Mod. Phys.* **50**, 191 (1978).
- <sup>87</sup>O. Sakai and Y. Kuramoto, *Solid State Commun.* **89**, 307 (1994).
- <sup>88</sup>R. Bulla, *Phys. Rev. Lett.* **83**, 136 (1999).
- <sup>89</sup>R. Bulla, T. Pruschke, and A. C. Hewson, *J. Phys.: Condens. Matter* **9**, 10463 (1997).
- <sup>90</sup>A. Georges, G. Kotliar, W. Krauth, and M. J. Rozenberg, *Rev. Mod. Phys.* **68**, 13 (1996).
- <sup>91</sup>R. Žitko, *Phys. Rev. B* **80**, 125125 (2009).
- <sup>92</sup>R. Žitko, *Comput. Phys. Commun.* **180**, 1271 (2009).
- <sup>93</sup>V. L. Campo and L. N. Oliveira, *Phys. Rev. B* **70**, 153401 (2004).
- <sup>94</sup>R. Žitko, *NRG Ljubljana*, <http://nrgljublana.ijs.si/> (2006).
- <sup>95</sup>R. Žitko, *Comput. Phys. Commun.* **182**, 2259 (2011).
- <sup>96</sup>R. Žitko and J. Bonča, *Phys. Rev. B* **73**, 035332 (2006).
- <sup>97</sup>A. I. Tóth, C. P. Moca, O. Legeza, and G. Zaránd, *Phys. Rev. B* **78**, 245109 (2008).
- <sup>98</sup>A. Weichselbaum, *Annals of Physics* **327**, 2972 (2012).
- <sup>99</sup>H. Hafermann, K. R. Patton, and P. Werner, *Phys. Rev. B* **85**, 205106 (2012).
- <sup>100</sup>L. R. Mead and N. Papanicolaou, *J. Math. Phys.* **25**, 2404 (1984).
- <sup>101</sup>R. N. Silver, D. S. Sivia, and J. E. Gubernatis, *Phys. Rev. B* **41**, 2380 (1990).
- <sup>102</sup>F. D. M. Haldane, *Phys. Rev. B* **15**, 281 (1977).
- <sup>103</sup>J. R. Schrieffer and P. A. Wolff, *Phys. Rev.* **149**, 491 (1966).
- <sup>104</sup>H. Suhl, *Phys. Rev.* **138**, A515 (1965).
- <sup>105</sup>D. C. Langreth, *Phys. Rev.* **150**, 516 (1966).
- <sup>106</sup>A. C. Hewson, *J. Phys.: Condens. Matter* **18**, 1815 (2006).
- <sup>107</sup>H. Shiba, *Prog. Theor. Phys.* **54**, 967 (1975).
- <sup>108</sup>L. Merker, A. Weichselbaum, and T. A. Costi, *Phys. Rev. B* **86**, 075153 (2012).
- <sup>109</sup>M. Karski, C. Raas, and G. S. Uhrig, *Phys. Rev. B* **72**, 113110 (2005).
- <sup>110</sup>M. Karski, C. Raas, and G. S. Uhrig, *Phys. Rev. B* **77**, 075116 (2008).
- <sup>111</sup>X. Deng, J. Mravlje, R. Žitko, M. Ferrero, G. Kotliar, and A. Georges, *Phys. Rev. Lett.* **110**, 086401 (2013).
- <sup>112</sup>H. O. Frota, *Phys. Rev. B* **45**, 1096 (1992).
- <sup>113</sup>R. Bulla, M. T. Glossop, D. E. Logan, and T. Pruschke, *J. Phys.: Condens. Matter* **12**, 4899 (2000).
- <sup>114</sup>D. E. Logan, M. P. Eastwood, and M. A. Tusch, *J. Phys.: Condens. Matter* **10**, 2673 (1998).
- <sup>115</sup>N. L. Dickens and D. E. Logan, *J. Phys.: Condens. Matter* **13**, 4505 (2001).
- <sup>116</sup>Y. Meir and N. S. Wingreen, *Phys. Rev. Lett.* **68**, 2512 (1992).